MODEL PREDICTIONS OF RADIATION STRESS PROFILES FOR NONLINEAR SHOALING WAVES

By

BRET M. WEBB

A THESIS PRESENTED TO THE GRADUATE SCHOOL
OF THE UNIVERSITY OF FLORIDA IN PARTIAL FULFILLMENT
OF THE REQUIREMENTS FOR THE DEGREE OF
MASTER OF SCIENCE

UNIVERSITY OF FLORIDA

2004

This work is dedicated to my wife, Shannon.

ACKNOWLEDGMENTS

First, I wish to thank my wife for her support and encouragement over the past few years. My parents, the rest of my immediate family, my extended family and circle of friends also deserve much credit for the person I have become, both socially and academically.

I would like to thank my advisor, Don Slinn, for his encouragement, ideas, and support. Drs. Robert G. Dean and Andrew Kennedy, of the University of Florida, deserve recognition for their service as members of my supervisory committee. Thanks go, also, to the remainder of the faculty and staff in the Department of Civil and Coastal Engineering. My office-mates, all of whom provided encouragement and guidance over the past few years, were instrumental in my success as a graduate student and they should be recognized for their contributions as well.

Todd Holland and Jack Puleo deserve acknowledgment for their support and encouragement, and for financial contributions that permitted me to attend various laboratory and field experiments over the past few years. Thanks should also be expressed to the Office of Naval Research and the University of Florida for providing financial support. A portion of this work, as well as my education, was made possible by the University of Florida Graduate Fellowship Initiative.

TABLE OF CONTENTS

LIST OF TABLES

LIST OF FIGURES

Abstract of Thesis Presented to the Graduate School
of the University of Florida in Partial Fulfillment of the
Requirements for the Degree of Master of Science

MODEL PREDICTIONS OF RADIATION STRESS PROFILES FOR NONLINEAR SHOALING WAVES

By

Bret M. Webb

December 2004

Chair: Donald N. Slinn
Major Department: Civil and Coastal Engineering

The flux of momentum directed shoreward by an incident wave field, commonly referred to as the radiation stress, plays a significant role in nearshore circulation and, therefore, has a profound impact on the transport of pollutants, biota, and sediment in nearshore systems. Having received much attention since the initial work of Longuet-Higgins and Stewart in the early 1960's, use of the radiation stress concept continues to be refined and evidence of its utility is widespread in literature pertaining to coastal and ocean science. A number of investigations, both numerical and analytical in nature, have used the concept of the radiation stress to derive appropriate forcing mechanisms that initiate cross-shore and longshore circulation, but typically in a depth-averaged sense due to a lack of information concerning the vertical distribution of the wave stresses.

While depth-averaged nearshore circulation models are still widely used today, advancements in technology have permitted the adaptation of three-dimensional (3-D) modeling techniques to study flow properties of complex nearshore circulation systems. It has been shown that the resulting circulation in these 3-D models is very sensitive

to the vertical distribution of the nearshore forcing, which have been implemented as either depth-uniform or depth-linear distributions. Recently, analytical expressions describing the vertical structure of radiation stress components have appeared in the literature, typically based on linear theory, but do not fully describe the magnitude and structure in the region bound by the trough and crest of nonlinear, propagating waves.

Utilizing a three-dimensional, nonlinear, numerical model that resolves the time-dependent free surface, we present mean flow properties resulting from a simulation of a laboratory experiment on uniform longshore currents. More specifically, we provide information regarding the vertical distribution of radiation stress components resulting from obliquely incident, nonlinear shoaling waves. Vertical profiles of the radiation stress components predicted by the numerical model are compared with published analytical solutions, expressions given by linear theory, and observations from an investigation employing second-order cnoidal wave theory.

CHAPTER 1
INTRODUCTION

1.1 Background

The nearshore coastal region, typically taken as the area between the instantaneous shoreline and a point just seaward of wave breaking, is a dynamic and complex system. As waves propagate into this area they release their energy into the water, forming currents that can persist in both the cross-shore and longshore directions. These currents, along with the coupling that takes place between the incident wave field and the currents, make up the nearshore circulation. Nearshore circulation continues to be studied and investigated as its importance is made evident through the transport of materials, organic and non-organic, in the coastal zone. Of paramount concern to the coastal scientist is the transport of sediment in the cross-shore and longshore directions, which continually acts to shape and reshape the nearshore seabed.

The study of nearshore circulation has been approached many different ways. Numerous laboratory and field experiments have been, and continue to be, performed in order to increase understanding of nearshore current dynamics. Analytical studies have paved the way for numerical simulations of nearshore processes and advances in computational science promote the development of comprehensive modeling tools. While two-dimensional (2-D) numerical models continue to be used for simulating nearshore circulations, several limitations are inherent in their application. Longshore-averaged 2-D models ignore the longshore variability of the wave climate and current systems, while depth-integrated 2-D models neglect the vertical structure of nearshore currents. Neither approach can provide complete information about sediment transport in the nearshore system: the first excludes the longshore degree of freedom while the latter ignores the vertical-dependence of the flow and sediment suspension

cannot be accurately described by depth-integrated quantities. The required coupling between separate shoaling wave models and phase-averaged circulation models becomes more complex in three dimensions. This coupling is guided by linear theory and empirically based approximations developed under idealized conditions. A standard approach is to solve a depth-integrated wave energy equation incorporating empirical formulations for wave energy dissipation. The transfer of momentum between the breaking waves and the mean currents is represented by radiation stress gradient terms. Distributing these forces appropriately over the water column represented in a phase-averaged, 3-D circulation model requires knowledge of their vertical distribution. The introduction of three-dimensional (3-D) wave-phase-averaged circulation models, however, has not provided the modeling panacea hoped for. The additional dimension demands enormous computational power and more comprehensive forcing techniques that require, in many cases, a priori knowledge of the flow field in all dimensions. Moreover, the circulation predicted by these models has been shown to be highly sensitive to the vertical distribution of forcing.

The term “radiation stress” describes the flow of momentum in propagating waves and is discussed at length in Longuet-Higgins and Stewart (1964). Incident waves provide the majority of momentum to the nearshore circulation. Gradients in the radiation stress fields represent the forcing applied to the surfzone. The vertical distribution of radiation stress over the water column affects the cross-shore and longshore circulation, as well as vertical mixing. Thus, choosing appropriate vertical distributions for the radiation stress terms is essential for accurate modeling of nearshore circulation.

Using a three-dimensional, finite-difference, Navier-Stokes model that resolves the time-dependent free surface, we perform simulations of a laboratory experiment of longshore currents. Mean flow properties of the simulation are then used to plot vertical profiles of the shoreward- and longshore-directed components of the

cross-shore radiation stress resulting from obliquely incident, nonlinear shoaling waves. Profiles of radiation stress are computed using a modified form of the equations suggested by Longuet-Higgins and Stewart (1964) and compared against profiles plotted using linear solutions presented in the literature. While we understand that this approach is neither the best nor the only way to model wave-current interactions, we hope to convey our findings in a manner that is helpful to other coastal scientists interested in these processes, especially those involved with the research and development of modeling tools.

1.2 Literature Survey

Apparent stress terms, which appear as velocity products in the convective acceleration terms found in the Navier-Stokes equations, and the radiation stress terms explicit in the wave energy equation, play significant roles in the resulting nearshore circulation in numerical models. Numerous theoretical, numerical, laboratory, and field studies have attempted to quantify or judge the relative importance of the normal and shear stresses resulting from shoaling and breaking waves. Recent attention has been given to the vertical distribution of these apparent stresses [see Deigaard and Fredsøe (1989); Sobey and Thieke (1989); and Rivero and Arcilla (1995)] and, more specifically, the radiation stresses that result from the incident wave field [Mellor (2003) and Xia *et al.* (2004)].

The pioneering work of Longuet-Higgins and Stewart (1964) is evident in most nearshore investigations and their concepts continue to be used and developed further. Unfortunately, this theoretical investigation relied heavily on the linear approximation of a propagating water wave and excluded contributions from the incident waves above the mean water level, citing the insignificance of the third-order integrands that result from extending the solution above the surface. Disregarding the contribution of the shoreward-directed momentum flux above the mean water level, according to Svendsen (1984) and Sobey and Thieke (1989), significantly underestimates the

magnitude of the radiation stress due to real, nonlinear propagating water waves. Also, the resulting analytical expressions presented in Longuet-Higgins and Stewart (1964) are depth-integrated quantities and, therefore, ignore potentially important vertical information. Contrary to the methodology followed by Xie *et al.* (2001), these depth-integrated quantities are not suitable for use as forcing terms in vertically dependent momentum equations. Traditional radiation stress expressions, however, have been used in both numerical and theoretical calculations, in depth-integrated form, to describe the wave-induced setup and setdown, as well as nearshore currents, and the results agree qualitatively with observations made by Badiei and Kamphuis (1995), Bowen *et al.* (1968), and Larson and Kraus (1991).

Recent attempts to provide three-dimensional radiation stress solutions have been made by Dolata and Rosenthal (1984), Mellor (2003), and Xia *et al.* (2004), but each has its limitations. Dolata and Rosenthal (1984) neglected pressure effects in their analytical solution, which, as we will show later, represent a significant component of the shoreward-directed component of the cross-shore radiation stress. The analytical solutions given by Mellor (2003) also employ linear wave theory and specifically address deep water propagating waves. In the context of nearshore circulation, where waves are often characterized as shallow water waves, these solutions do not appear to be appropriate. Xia *et al.* (2004) begin with the depth-integrated equations for radiation stress presented by Longuet-Higgins and Stewart (1964), disregard the vertical integration of the terms, and then substitute linear expressions for the velocity and pressure terms into the modified equations.[1] The resulting analytical solutions given by Xia *et al.* (2004) are ultimately limited by their small-amplitude assumption—that

[1] While the solutions of Xia *et al.* (2004) were considered in this investigation, the resulting profiles computed with their expressions are not presented in our results because they were similar to the profiles computed with the expressions of Mellor (2003).

is, the ratio of wave amplitude to wavelength is much less than unity. In the shallow waters of the nearshore system, it is not uncommon for this assumption to be violated as the wave amplitude increases through shoaling and the wavelength decreases to satisfy the linear dispersion relationship. When small-amplitude assumptions are employed in this manner, analytical solutions based on them begin to differ from observations and errors are inherent in subsequent calculations (Stive and Wind, 1982). Finite-amplitude and cnoidal wave theories provide better estimates of wave velocities in shallow waters (Xia *et al.*, 2004). The vertical distributions of apparent stress terms (velocity products), explicit in the classical radiation stress expressions given by Longuet-Higgins and Stewart (1964), resulting from an investigation employing second-order cnoidal wave theory were presented in Sobey and Thieke (1989). Although they did not provide three-dimensional radiation stress solutions, comments and observations regarding their investigation prove useful to our study of the Eulerian mean flow and the resulting vertical profiles.

1.3 Organization

In the chapters that follow, we provide information about the vertical distributions of velocity and momentum, and the net effects from obliquely incident, monochromatic waves on a Eulerian mean flow. Characteristics, abilities, and limitations of the numerical model used in this study are presented in Chapter 2; the governing equations and improved boundary conditions for forcing and free surface velocities are discussed here as well. In Chapter 3, we provide a brief summary of the laboratory experiments [Visser (1984), Visser (1991)] used to validate model predictions, explain how the model was adapted to simulate the experiment, and discuss physical and numerical results of performing such a simulation with the model. The results of the model-data comparison and subsequent simulations are provided in Chapter 4, along with analysis of the model predictions. This analysis ultimately leads to discussion of the vertical distribution of radiation stress, also presented in Chapter 4, where we compare

predicted profiles from the nonlinear model to the distributions suggested by analytical solutions found in the literature. Concluding remarks on the capability of the numerical model to reproduce nearshore processes and a summary of findings on the vertical distribution of radiation stress for nonlinear shoaling waves are given in Chapter 5. Details concerning the theta-weighted, finite-differencing schemes and the sensitivity of model predictions to the differencing schemes used are presented in Appendix A. A discussion on the cross-shore mass balance is found in Appendix B where we provide additional information to support our claim that the numerical model is conservative.

CHAPTER 2
METHODOLOGY

2.1 Model Characteristics

The numerical model considered, SOLA-SURF, is a three-dimensional model that employs computational fluid dynamics (CFD) to describe unsteady fluid flows. SOLA-SURF is an extension of a two-dimensional CFD model, SOLA, that was created to study time-dependent fluid flows in confined regions. Alternate extensions of the original SOLA code have been used to study processes such as buoyancy-driven flows, flows of stratified fluids, and flows in porous media (Hirt *et al.*, 1975). In contrast to the original model, SOLA-SURF has the ability to model fluid flows bound by free or curved rigid surfaces. The addition of these surface boundary conditions permits the user to simulate water wave propagation over variable bathymetry. Various lateral boundary conditions may be used in the model: possible configurations include free-slip and no-slip walls, continuative or outflow boundaries, and periodic boundary conditions. The discretised equations of motion may be solved on either axisymmetric or Cartesian coordinate systems. There are no physical, empirical coefficients to tune and few numerical coefficients to define in this model, making the code adaptable to a broad range of applications.

SOLA-SURF is based on the Marker-and-Cell (MAC) method where the primary dependent variables, pressure and velocity, are solved in a Eulerian reference frame. Characteristic of MAC schemes, a staggered grid is used to define the locations of the pressure and the three components of velocity. On this grid, the pressure is defined at the center of each control volume while the components of velocity are located on cell faces. A typical grid cell used in MAC schemes is shown in Fig. 2–1, where the orientation of the coordinate axes is representative of the system used in SOLA-SURF.

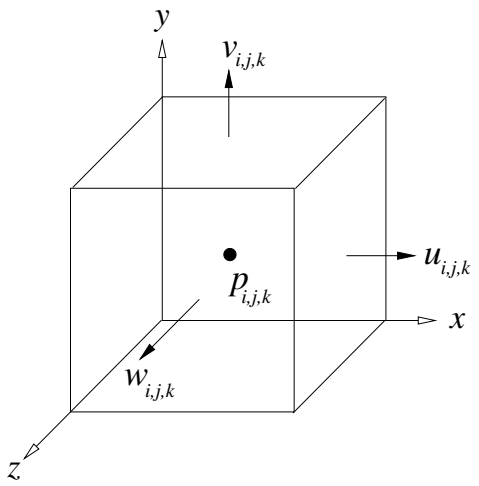

Figure 2–1: A typical computational cell used in a staggered grid and the associated coordinate axis system.

A Cartesian coordinate system (x, y, z) represents the cross-shore, vertical, and longshore directions, respectively, and simulations are performed on a rectangular grid.

2.2 Governing Equations

SOLA-SURF solves the Navier-Stokes equations (Eqs. 2–2, 2–3, and 2–4) in discretised form and satisfies the mass continuity equation (Eq. 2–1) through the incorporation of a Poisson equation for the pressure field. In the context of this work, the equations of motion characterize an unsteady, incompressible, homogeneous fluid. Our Cartesian coordinate system associates the x, y, and z directions with the u, v, and w velocity components, respectively.

$$\frac{\partial u}{\partial x} + \frac{\partial v}{\partial y} + \frac{\partial w}{\partial z} = 0 \tag{2–1}$$

$$\frac{\partial u}{\partial t} + \frac{\partial u^2}{\partial x} + \frac{\partial uv}{\partial y} + \frac{\partial uw}{\partial z} = -\frac{\partial p}{\partial x} + \nu \left[\frac{\partial^2 u}{\partial x^2} + \frac{\partial^2 u}{\partial y^2} + \frac{\partial^2 u}{\partial z^2} \right] \tag{2–2}$$

$$\frac{\partial v}{\partial t} + \frac{\partial uv}{\partial x} + \frac{\partial v^2}{\partial y} + \frac{\partial vw}{\partial z} = -\frac{\partial p}{\partial y} + \nu \left[\frac{\partial^2 v}{\partial x^2} + \frac{\partial^2 v}{\partial y^2} + \frac{\partial^2 v}{\partial z^2} \right] + g \qquad (2\text{–}3)$$

$$\frac{\partial w}{\partial t} + \frac{\partial uw}{\partial x} + \frac{\partial vw}{\partial y} + \frac{\partial w^2}{\partial z} = -\frac{\partial p}{\partial z} + \nu \left[\frac{\partial^2 w}{\partial x^2} + \frac{\partial^2 w}{\partial y^2} + \frac{\partial^2 w}{\partial z^2} \right] \qquad (2\text{–}4)$$

where
$g =$ gravitational acceleration
$\nu =$ coefficient of kinematic viscosity

Following from the assumption that the fluid is incompressible and homogeneous, pressure in the model is defined as the ratio of pressure to constant density. Simulations are performed with a rigid bottom boundary that best represents the bathymetry of our problem. The initial pressure field for a fluid at rest is hydrostatic, which we use to initialize simulations starting from an equilibrium state where no motion exists. Once the simulations begin, the model uses the two-step projection method of Chorin (1968) to solve for the pressure field. The intermediate step velocity projection fields are found by substituting the initial pressure and velocity fields into the discretised equations of motion that utilize a theta scheme to control the amount of donor cell differencing for the convective flux terms. The viscous flux terms are discretised using a three-point stencil that yields second-order central differences. Boundary conditions are then applied to the velocity field and cell pressures are adjusted iteratively in order to satisfy the mass continuity equation (Eq. 2–1). If the divergence of the velocity field in a cell (the left hand side of Eq. 2–1) is less than zero, the pressure of that cell is increased to decrease the flow of mass into the cell; the converse of this statement is also true and the cell pressure is decreased to encourage the flow of mass back into a cell when the divergence of the cell is greater than zero. Since the MAC scheme uses only one point to approximate the pressure of each cell, the divergence of the velocity field may be driven to zero, or to a desired level of accuracy, in an iterative manner. Typical values of the convergence criteria, ϵ, are on the order of 10^{-3} or

smaller (Hirt *et al.*, 1975). In order to decrease the number of iterations required to satisfy ϵ, an over-relaxation factor, Ω, is applied to the predicted pressure differential. Finding an optimal value of the over-relaxation factor requires, in part, performing a rather exhaustive eigenvalue expansion of the system of equations—a task that we do not seek to undertake (Fletcher, 2000). Therefore, following guidance provided by the SOLA manual we take the over-relaxation factor to be 1.8, which is still well below the stability threshold of 2.0. While successive over-relaxation (SOR) methods typically decrease the number of iterations required to reach some desired level of convergence, they can become computationally expensive for increasing numbers of grid cells. Additional information regarding the effect of SOR on computational time is presented in Chapter 3.

Contrary to some MAC formulations, SOLA-SURF does not employ marking particles to track the free surface. Instead, the location of the free surface is predicted by substituting velocity predictions provided by the momentum equations into the kinematic free surface boundary condition. Once the continuity equation has been satisfied, the resulting velocity field is then used in conjunction with the kinematic free surface boundary condition (KFSBC) to determine the time-dependent free surface, providing unique three-dimensional representations of the fluid surface throughout a simulation. The KFSBC is given by Eq. 2–5, where the free surface is defined as the height, ζ, of the surface above the rigid bottom boundary.

$$\frac{\partial \zeta}{\partial t} + u\frac{\partial \zeta}{\partial x} + w\frac{\partial \zeta}{\partial z} = v \tag{2–5}$$

The discretised form of the KFSBC employs an alternative theta scheme (independent of that used in the convective acceleration terms) to control the amount of donor cell differencing, and uses a one-step projection method to predict the free surface location at the newest time-level. In the context of our simulations, we have found it advisable to use second-order central differences in the spatial discretisation of

Eq. 2–5. Additional information regarding the predictive skill of various discretisation schemes, as well as examples of the discretised forms of a convective acceleration term and the KFSBC are presented in Appendix A.

The free surface in SOLA-SURF must be definable by a single point in both horizontal directions. This constraint arises from the simplified approach used to solve the discretised equations of motion, the KFSBC, and also the cell pressures. Water waves exhibiting this type of surface feature are often classified as *spilling breakers* at the limit of breaking (Dean and Dalrymple, 1991) as the slope of the fluid surface never reaches infinity (vertical). Since SOLA-SURF does not allow the slope of the free surface to exceed the cell aspect ratio, either $\delta y/\delta x$ or $\delta y/\delta z$, the model is unable to resolve plunging breakers or other complex, multi-valued free surfaces. The breaker type is often classified by the surf similarity parameter (ξ), first used by Iribarren and Nogales (1949), and is defined in Eq. 2–6.

$$\xi = \frac{\tan\alpha}{\sqrt{\frac{H}{L_o}}} \tag{2–6}$$

where
$\alpha =$ slope of bathymetry
$H =$ wave height
$L_o =$ deep-water wavelength

For waves traveling at oblique angles, the surf similarity parameter is changed slightly, yielding the inshore surf similarity parameter—ξ_{br}—of Battjes (1974) shown in Eq. 2–7.

$$\xi_{br} = \frac{\tan\alpha}{\sqrt{\frac{H_{br}}{L_o}}}\cos\theta_{br} \tag{2–7}$$

where
$\theta_{br} =$ wave angle at breaking
$H_{br} =$ wave height at breaking

The classification of breaking wave types, also presented by Battjes (1974), is given in Table 2–1.

Table 2–1: Breaking wave types classified by the inshore surf similarity parameter.

surging or collapsing if	$\xi_{br} > 2.0$
plunging if	$0.4 < \xi_{br} < 2.0$
spilling if	$\xi_{br} < 0.4$

2.3 Improved Boundary Conditions

2.3.1 Wave Forcing

A new forcing method was added to SOLA-SURF and is applied as a time-dependent offshore boundary condition. This method specifies both the potential and kinetic energy of a monochromatic wave at the offshore boundary. This implies that both the free surface and velocity are forced at the boundary. The equations for the free surface (Eq. 2–8) and the three-dimensional velocity potential (Eq. 2–9) were suggested by Boccotti (2000).

$$\eta(x,z,t) = \frac{H}{2}\cos\left(kz\sin\theta + kx\cos\theta - \omega t\right) \tag{2–8}$$

$$\phi(x,y,z,t) = \frac{H}{2}g\omega^{-1}\frac{\cosh k(h+y)}{\cosh kh}\sin\left(kz\sin\theta + kx\cos\theta - \omega t\right) \tag{2–9}$$

where
$H =$ wave height
$k =$ wavenumber
$h =$ water depth
$\theta =$ wave angle with respect to shore normal
$\omega =$ angular frequency
$t =$ time

Assuming that the model describes irrotational incident waves, a velocity potential for the fluid exists and the total fluid velocity is described by Eq. 2–10.

$$\vec{u} = \nabla\phi \tag{2–10}$$

Combining this with the assumption that the fluid is incompressible (Eq. 2–11)

$$\nabla\cdot\vec{u} = 0 \tag{2–11}$$

enforces the Laplacian of the velocity potential to be equal to zero. This constraint is found by substituting Eq. 2–10 into Eq. 2–11, which gives Eq. 2–12.

$$\nabla^2 \phi = 0 \tag{2–12}$$

The three components of velocity used to force the wave signal are derived from the velocity potential using Eq. 2–10 and are given by

$$u = \frac{\partial \phi}{\partial x}, \quad v = \frac{\partial \phi}{\partial y}, \quad \text{and} \quad w = \frac{\partial \phi}{\partial z}$$

and the resulting forcing equations for the velocity components are given by Eqs. 2–13, 2–14, and 2–15.

$$u(x, y, z, t) = \frac{H}{2} g k \omega^{-1} \frac{\cosh k(h + y)}{\cosh kh} \cos\left(kz \sin\theta + kx \cos\theta - \omega t\right) \cos\theta \tag{2–13}$$

$$v(x, y, z, t) = \frac{H}{2} g k \omega^{-1} \frac{\sinh k(h + y)}{\cosh kh} \sin\left(kz \sin\theta + kx \cos\theta - \omega t\right) \tag{2–14}$$

$$w(x, y, z, t) = \frac{H}{2} g k \omega^{-1} \frac{\cosh k(h + y)}{\cosh kh} \cos\left(kz \sin\theta + kx \cos\theta - \omega t\right) \sin\theta \tag{2–15}$$

Graphical representations of the velocity fields are presented in Fig. 2–2.

SOLA-SURF requires only basic wave parameters to force the monochromatic wave signal. The wave amplitude, period, and direction must be specified along with the water depth. Using this information the model computes the values of η, u, v, and w using the preceding expressions. These values are specified in the first grid cell, for each time step, and the equations of motion then govern the propagation of the wave throughout the domain. The length of the cross-shore domain and the boundary condition used near the onshore boundary result in minimal reflected waves traveling back offshore. This allows the incident waves to retain a consistent shape and

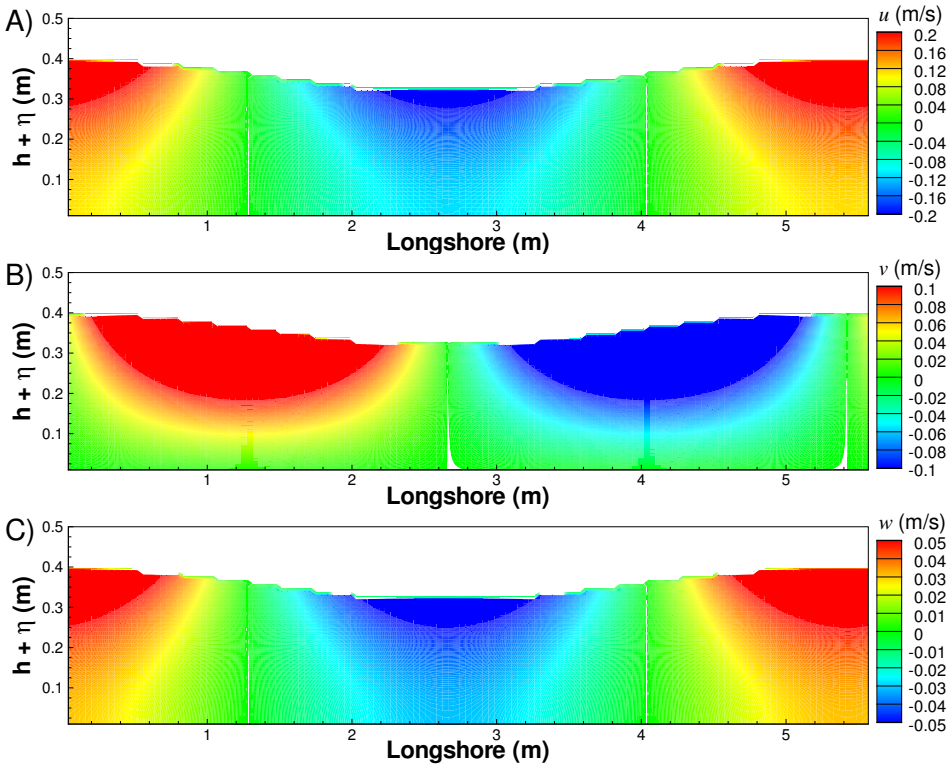

Figure 2–2: Contour plots of the velocity fields at the forcing boundary derived from the three-dimensional velocity potential equation for an incident angle of $\theta = 15.4°$. The velocity contours of A) u, B) v, and C) w demonstrate the depth-dependency of the linear equations.

magnitude throughout a simulation, thereby eliminating the need to tune or adjust the time-dependent boundary conditions to allow for outgoing wave characteristics.

2.3.2 Free Surface Velocity Boundary Conditions

The velocity boundary conditions for the free surface must be treated differently than the lateral boundaries in the model and require special attention. A modified free-slip condition is specified on the free surface,

$$\frac{\partial u}{\partial y} = 0 \qquad \frac{\partial w}{\partial y} = 0 \qquad \frac{\partial v}{\partial y} = -\left(\frac{\partial u}{\partial x} + \frac{\partial w}{\partial z}\right)$$

which prohibits shear in the velocity field across the fluid interface and solves for the vertical component of velocity (v) in a manner that explicitly satisfies the mass continuity equation (Eq. 2–1). The boundary conditions applied to the horizontal

velocity components near the free surface, using ghost points, are discretised as

$$u_{i,jt,k} = u_{i,jt-1,k} \quad \text{and} \quad w_{i,jt,k} = w_{i,jt-1,k}$$

where the index notation jt is used to represent the uppermost grid cell containing the free surface. While appropriate for a mildly sloping free surface, these boundary conditions must be altered for the limiting case of maximum steepness: when the slope of the free surface approaches the cell aspect ratio. When the slope of the free surface approaches this limit, the horizontal velocity components in the cell containing the free surface are set using a method that produces vertical momentum transfer [see Chen *et al.* (1995)]. Demonstrated in panel B of Fig. 2–3, the improved methods for prescribing the horizontal velocity boundary conditions are given by

$$u_{i,jt,k} = u_{i-1,jt,k} \quad \text{and} \quad w_{i,jt,k} = w_{i,jt,k-1}.$$

This improved method, suggested by Chen *et al.* (1995), better represents a free-slip condition when the slope of the free surface nears the limit of maximum steepness. While only the u velocity is depicted in Fig. 2–3, a similar prescription is applied to the orthogonal horizontal velocity component w.

Where the original velocity boundary conditions satisfy the free-slip condition for a mildly sloping surface, it is observed that by neglecting vertical gradients of the horizontal velocity components

$$\frac{\partial u}{\partial y} = 0 \quad \text{and} \quad \frac{\partial w}{\partial y} = 0$$

in the case of maximum steepness, there is little momentum transfer from the spilling wave into the water column. Since SOLA-SURF does not use a subgrid model to simulate wave breaking, and in the absence of a parameterization for energy dissipation due to wave breaking, the improved velocity boundary conditions provide a sufficient mechanism to promote momentum transfer from the wave to the mean flow. The

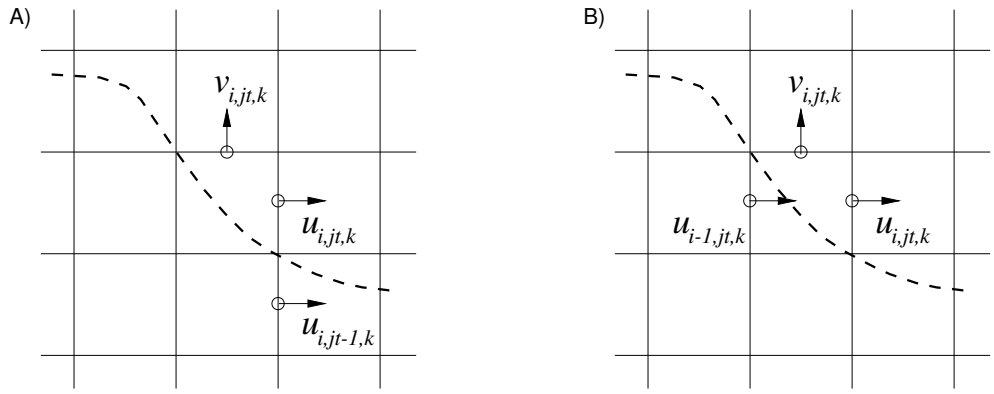

Figure 2–3: Special cases for setting the velocity components on the free surface, represented here by the dashed line. A) is the original method employed by the model and B) is the improved method.

effects of these velocity boundary conditions on the generation of longshore currents and wave transformation are discussed in Chapter 4.

2.3.3 Rigid Bottom Velocity Boundary Conditions

A no-slip boundary condition is applied to the rigid bottom boundary, requiring that the horizontal velocity components equal zero at the bed. The velocity component normal to the bed is also set equal to zero since flow is not permitted to cross the rigid bottom boundary. These conditions, prescribed using ghost points outside of the computational domain, are given by

$$u_{i,jb-1,k} = -u_{i,jb,k}, \quad w_{i,jb-1,k} = -w_{i,jb,k}, \quad \text{and} \quad v_{i,jb-1,k} = 0$$

where jb is the index of the vertical grid cell containing the bottom boundary. Using these prescriptions for the horizontal velocity components forces their value to be zero at the bed.

For simulations performed on a rectangular grid, a sloping boundary is represented by a series of small steps. Additional information about the behavior of horizontal

velocity components around these steps must be supplied to the model. Fig. 2–4 is a schematic of a single step in the rigid bottom boundary. The velocity boundary conditions used around a step are

$$u_{i,jb,k} = 0 \quad \text{and} \quad u_{i,jb-1,k} = 0$$

which states that flow is not permitted to cross the bottom boundary. Similar prescriptions are used for the w velocity component. For bathymetry that does not vary in the longshore (z) direction, only the no-slip condition on the boundary must be specified.

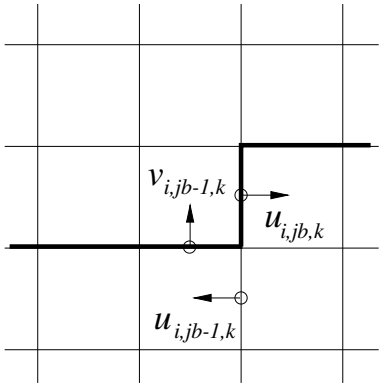

Figure 2–4: Prescriptions for setting the tangential velocity components around a step. The dark black line represents the rigid bottom boundary.

CHAPTER 3
EXPERIMENTS

In order to determine the ability of SOLA-SURF to predict nearshore processes such as wave transformation and the generation of longshore currents, simulations of a laboratory experiment were conducted. A series of laboratory experiments conducted by Visser (1984) were performed in a range of wave and basin parameters suitable for simulating with our model. In particular, we chose to simulate his Experiment 4 with SOLA-SURF for its unique set of parameters and for the accompanying comprehensive data set presented in Visser (1991).

3.1 Visser Experiment

The purpose of Visser's laboratory experiment was twofold: first, he sought to develop a method for generating uniform longshore currents in a laboratory setting and second, to provide scientists with a large set of data characterizing longshore currents for approximately longshore-uniform conditions. Visser evaluated a number of wave basin configurations before electing to use a basin with a pumped recirculation system. This recirculation system provided a stabilizing mechanism for the longshore uniformity of the currents and care was taken to determine appropriate pumping rates. Detailed information regarding the wave basin and the recirculation system may be found in Visser (1984) and Visser (1991).

Numerous experiments were conducted using a variety of wave parameters, two different beach slopes, and two distinct beach surfaces. One experiment in particular—Experiment 4—was performed with a set of parameters conducive to performing simulations with SOLA-SURF. There is also a significant amount of data presented in Visser (1991) that corresponds to this experiment. The parameters used in Experiment 4 are presented in Table 3–1, where α is the beach slope angle, T is the

Table 3–1: Beach and wave parameters used in Visser's Experiment 4.

$\tan\alpha$	T (s)	d (cm)	θ (degr)	H (cm)
0.050	1.02	35.0	15.4	7.8

wave period, d is the still water depth at forcing, θ is the wave angle at forcing, and H is the forced wave height.

3.2 Model Formulation

The total dimensions of Visser's wave basin—34 m longshore by 16.6 m cross-shore—were quite large in comparison to the wavelength and wave height associated with the experiment. In order to reduce the size of the computational domain used in the simulations of Visser's experiment, only the sloping part of the basin is included in the model bathymetry and the longshore extent of the domain is equivalent to the longshore wavelength of the forced waves. As discussed in Chapter 2, waves are forced by applying time-dependent boundary conditions on the free surface (Eq. 2–8) and the three velocity components (Eqs. 2–13–2–15). These wave forcing boundary conditions are applied at the location $x = 0$ m in Fig. 3–1. In order to simulate obliquely incident waves similar to those created in the lab, periodic boundary conditions are used in the longshore (z) direction of the computational domain. These periodic conditions, as compared to free or no-slip walls, prevent wave reflection from the lateral boundaries and result in a consistent wave field. Enforcing periodic longshore boundary conditions in SOLA-SURF requires the longshore extent of the domain to equal the longshore component of the wavelength. The wavelength may be found by solving the linear dispersion relationship for the wavenumber—k—in an iterative fashion. The linear dispersion relationship is given in Eq. 3–1.

$$\omega^2 = gk \tanh kh \tag{3–1}$$

In this case, k represents the wavenumber magnitude. For obliquely incident waves, the wavenumber magnitude is the resultant of the cross-shore and longshore wavenumber components, which are given by the following expressions

$$k_x = k\cos\theta \qquad k_z = k\sin\theta \quad ,$$

where θ is the local angle of wave incidence measured from the shore-normal direction.

The parameters of the experiment, combined with the periodicity requirement, result in typical physical domain lengths of about 10 m in the cross-shore, approximately 5.6 m in the longshore and 0.5 m in the vertical direction. A representative domain is shown in Fig. 3–1. In order to accurately resolve wave parameters, grid cells were chosen to be 0.01 m in the vertical and 0.04 m in the horizontal directions. These length scales result in a computational domain containing nearly 1.75 million grid cells; however, since the model does not compute values below the bottom boundary, about one-half of those cells remain unused.

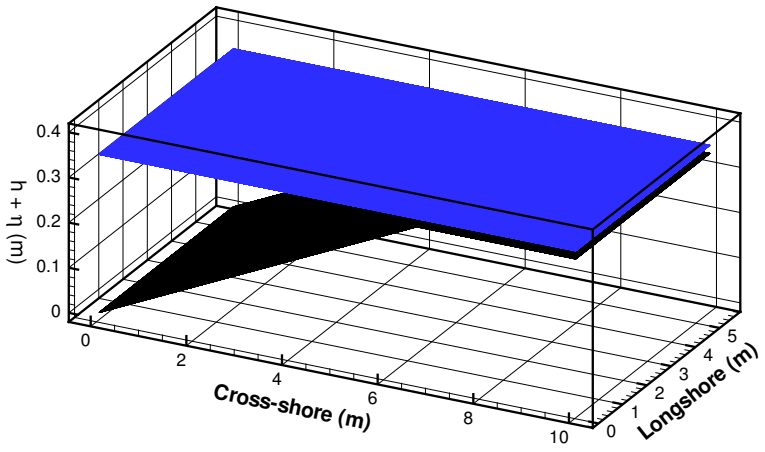

Figure 3–1: Physical domain used in the simulation of Visser's Experiment 4 showing the bathymetry, still water level, and domain lengths.

3.3 Model Simulations

3.3.1 Numerical Convergence

A variety of grid resolutions were tested during simulations of Visser's experiment to ensure that numerical convergence had been reached. The five different grid resolutions (Table 3–2) were also used to determine the effect of the cell aspect ratio on the prediction of cross-shore wave heights, which is demonstrated in Fig. 3–2. Nearly all of the predicted root-mean-square (RMS) wave heights from various grid resolutions fall within one standard deviation of the mean value. We chose to perform simulations with a cell aspect ratio of 1:4, in order to enhance the predictive ability of SOLA-SURF and to minimize the computational cost of running a simulation.

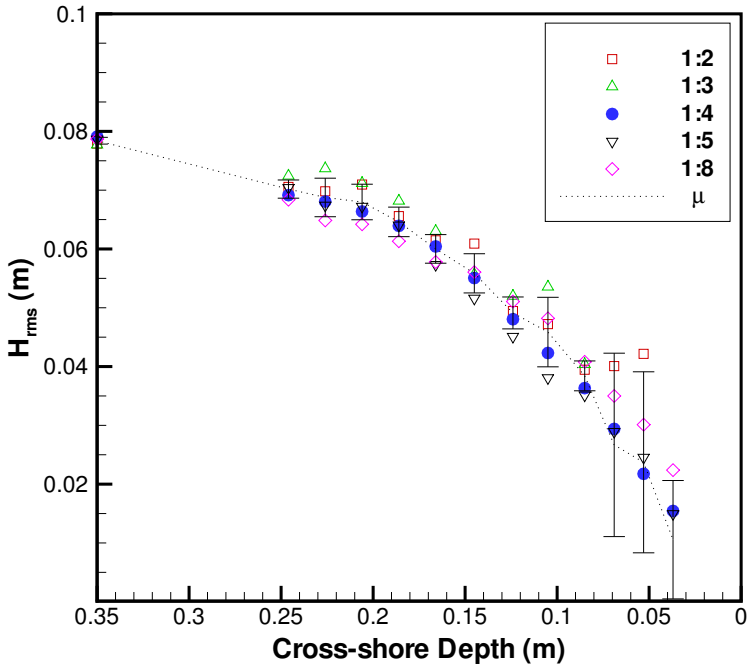

Figure 3–2: Predicted root-mean-square wave heights for five different grid resolutions. The dotted line represents the mean of the predictions at each cross-shore location and the error bars signify ± one standard deviation from the mean.

3.3.2 Computational Cost

As noted in Chapter 2, the SOR method applied to the pressure solver reduces the number of iterations necessary to satisfy the convergence criterion, but increases the total computational time as each iteration takes longer to perform. The simulations performed to investigate the effect of grid resolution are presented in Table 3–2, along with the number of hours required to complete one full, 200 s simulation of Visser's experiment. A graphical representation of the data presented in Table 3–2 is shown in Fig. 3–3, where the data has been plotted on a log-log plot to demonstrate the relationship between the number of computational grid cells and the time required to complete a simulation.

Table 3–2: Summary of simulations performed to investigate numerical convergence and computational cost.

Cell Aspect Ratio ($\delta y : \delta x$)	Grid Cell Distribution (nx, ny, nz)	Elapsed Time (hrs)
1:8	125, 50, 70	67
1:5	200, 50, 100	133
1:4	250, 50, 140	233
1:3	265, 50, 185	400
1:2	400, 50, 280	2000

3.3.3 Compensating for Mass Flux

Finite amplitude water waves produce a mean transport of mass, or mass flux, in the direction of propagation. This mass transport, in a Eulerian sense, stems from the difference in fluid volume contained under the wave crest and wave trough. In the context of our model, if the velocities at the forcing boundary were left in their original form there would be an increase of mass in the computational domain. In order to counteract this mass flux at the forcing boundary, the forcing velocities must be altered in some cogent manner.

We allowed the model to run for a number of wave periods (usually ten) without applying corrections to the forcing velocities and calculated their depth and

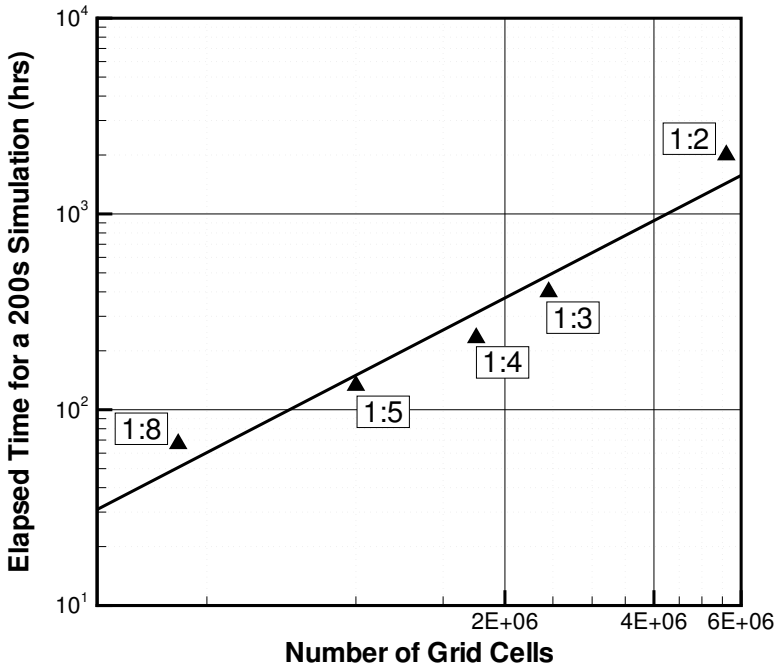

Figure 3–3: Computational time required for various grid resolutions. The diagram shows the logarithmic increase in computational cost as a function of the number of computational grid cells. The power-fit line is of the form $y = e^{(A\,log(x)+B)}$.

longshore-averaged values at a frequency of ten hertz. By then taking a time-average of the velocity components over the ten wave periods, we find the excess velocity due to mass transport. These excess velocity values are then subtracted from their respective forcing velocity components, uniformly over depth and time, and the simulation is started from rest and allowed to run to steady-state. The effects of mass flux on the fluid surface as a function of time is shown in Fig. 3–4. The dotted red line in this figure represents the fluid surface as a function of time for a simulation without mass flux velocity corrections. Comparing the average trend of this series ($\mathrm{H_{avg}}$) to the analytical solution provided by linear theory (Dean and Dalrymple, 1991), which is given by the thin, dashed black line, yields an agreeable result. The resulting average fluid surface after the velocity corrections have been applied is given by the dashed and

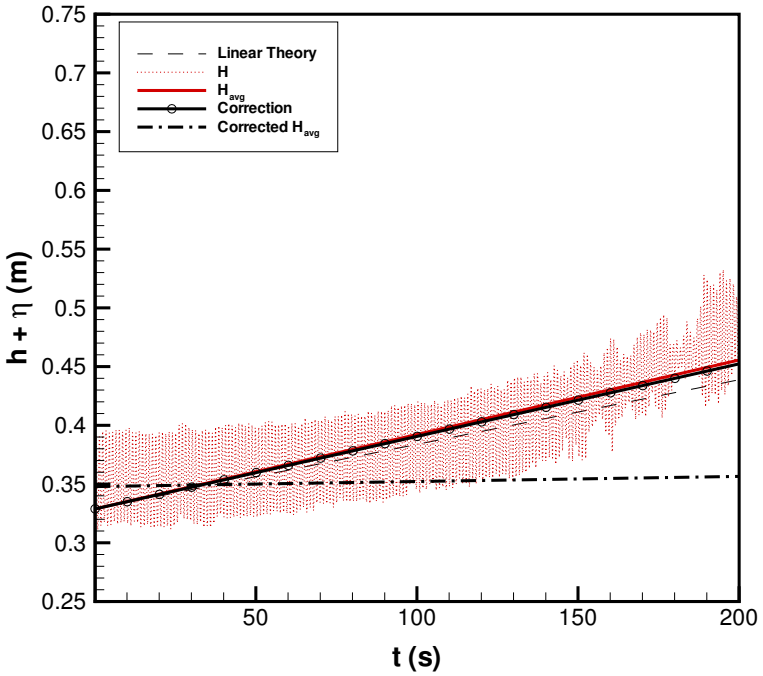

Figure 3–4: The response of the fluid surface, H, to mass flux near the forcing boundary, (x, z)=$(0.01, 2.0)$ m. A time series of H for a simulation without velocity corrections is represented by the dotted red line. The solid red line is the average trend of the surface H(t), and the velocity corrections calculated predict a fluid-surface rise given by the solid black line with circles. The dashed, thin black line is the analytical solution given by linear theory and the dash-dot, dark black line represents the corrected surface H(t).

dotted black line, which remains at a constant elevation of 0.35 m above the bottom boundary.

3.3.4 Nonlinearity of Model Predictions

The time-dependent boundary conditions applied on the velocity field to force the oblique, monochromatic wave signal were derived from a linear velocity potential equation. Water surface displacements near the forcing boundary, therefore, are sinusoidal in form and so are the velocity fields. The momentum equations (Eqs. 2–2–2–4) that govern the propagation of the wave signal throughout the domain are nonlinear equations and provide, accordingly, nonlinear developments to the

velocity field. These linear and nonlinear characteristics are demonstrated in panels B and C of Fig. 3–5. The 30 s time-series of the velocity components was taken from the full 200 s time-series recorded during the simulation at an inshore point in shallow water and is denoted by the dark black box in panel A.

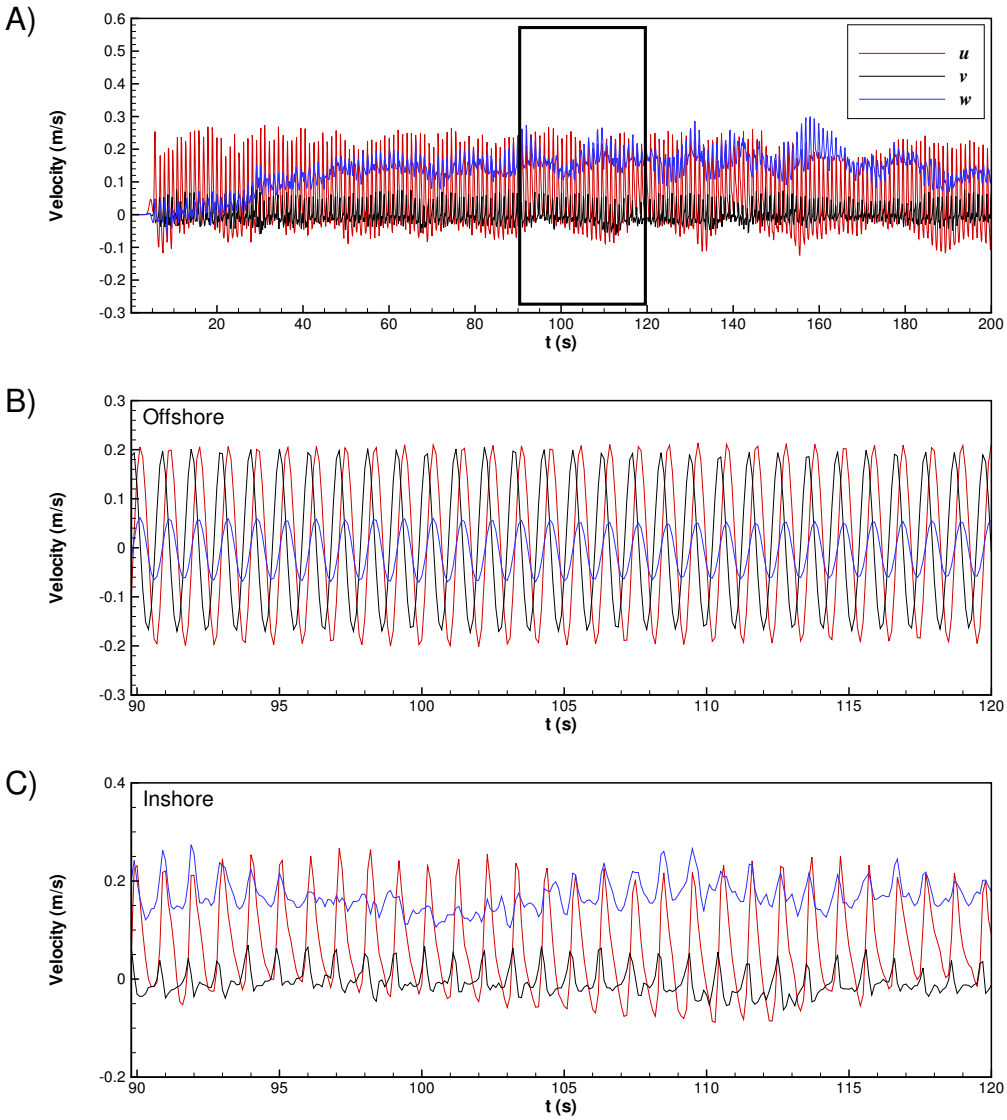

Figure 3–5: Contrasting velocity time-series plots taken at offshore (0.2 m, 0.28 m, 2.0 m) and inshore (5.6 m, 0.3 m, 2.0 m) locations. A) shows the complete, 200 s time-series of u, v, and w taken at the inshore point. B) is a 30 s time-series of the three velocity components near the forcing boundary. C) shows the nonlinearity and asymmetry of the velocity components over a 30 s time-series taken in 3 cm of water.

CHAPTER 4
RESULTS

4.1 Model-Data Comparison

Performing simulations of Visser's Experiment 4 allows us to evaluate the predictive skill of SOLA-SURF by comparing predicted nearshore processes to those observed and measured in the laboratory. A significant amount of data representing wave transformation and the formation of longshore currents is provided by Visser (1991) and serve as benchmarks to assess the capabilities of our model.

4.1.1 Wave Transformation

The predicted free surface elevations, taken from a transect through the middle of the longshore domain, are recorded at a frequency of 10 Hz throughout a simulation. A time-series corresponding to approximately ten wave-periods is then taken from the total record and analyzed to compute wave height statistics. The mean of the time-series is calculated and subsequently removed from the data, resulting in positive and negative oscillations about zero. A zero down-crossing technique is then used to extract individual wave events from the record, thereby allowing us to calculate statistical properties associated with the wave record. These statistical properties are presented in Fig. 4–1, where we compare the predicted significant wave heights (H_s), maximum wave heights (H_{max}), and RMS wave heights (H_{rms}), to the wave heights measured during the lab experiment.

Performing simulations with the original free-slip surface velocity boundary conditions produced wave heights that were similar in magnitude to those measured in the experiment. Simulations performed with the original free-slip boundary conditions, however, produced longshore current velocities that were only about 10% of the expected values. As suggested in Chapter 2, the original velocity boundary

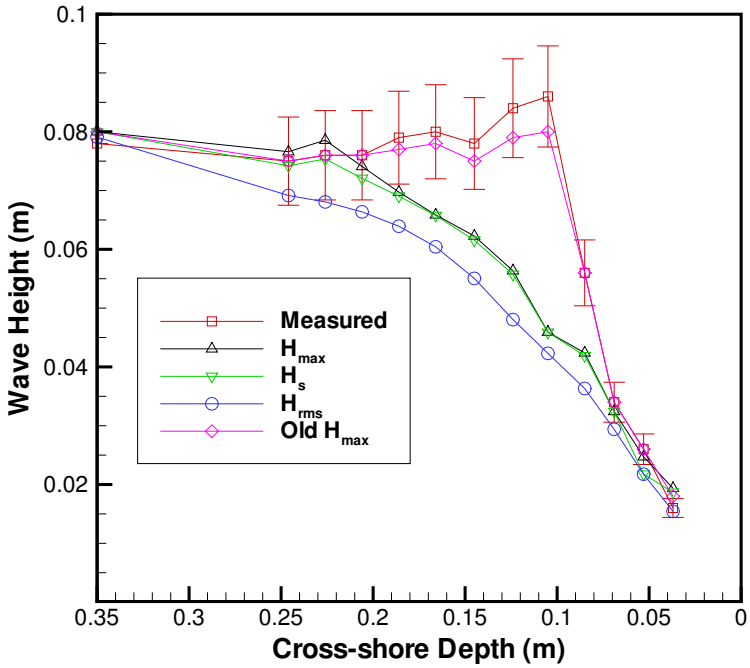

Figure 4–1: Comparison of measured (red) and predicted wave heights as a function of the cross-shore depth. The error bars represent possible measurement errors of $\pm$ 10%, suggested in Visser (1991). The data points corresponding to the label *Old* H_{max} were predicted by SOLA-SURF using the original free surface velocity boundary conditions. H_{max}, H_s, and H_{rms} represent the predicted maximum, significant, and root mean square wave heights, respectively.

conditions neglected vertical gradients in the velocity field across the free surface, thereby prohibiting momentum transfer from the steepening wave to the mean flow. Simulations implementing the improved free surface velocity boundary conditions (Chen *et al.*, 1995) provide reasonable estimates of the longshore current velocities, but under-predict the shoaling wave heights. Demonstrated in Fig. 4–1, the RMS wave heights predicted by the model are smaller than the average values collected during the experiment. The comparison shows reasonable agreement for the first few data points, those in deeper water, and also for the last few data points, but demonstrates the inability to accurately reproduce the shoaling wave heights observed in the experiment. A possible explanation for the large differences between the measured and predicted

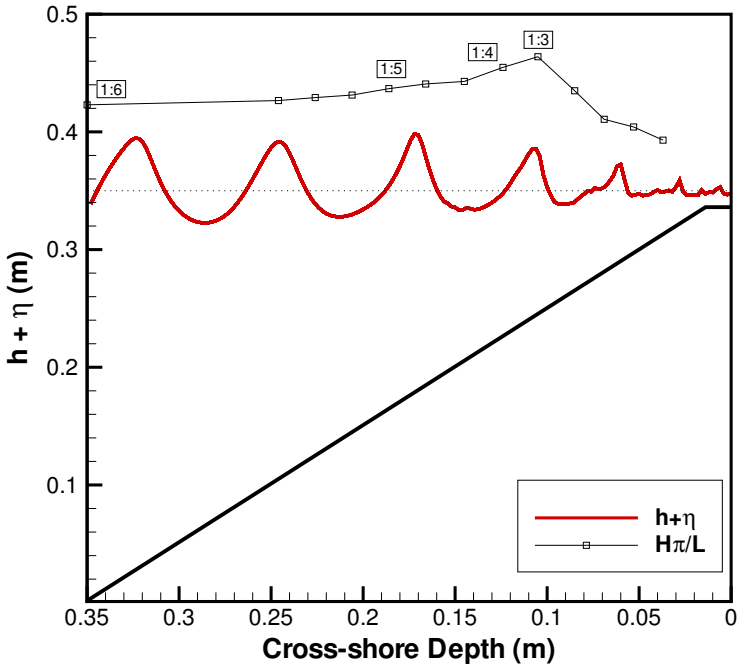

Figure 4–2: The instantaneous free surface and wave steepness. A transect taken near the midpoint of the longshore domain shows the instantaneous free surface (h+η), bathymetry (solid black line), and the approximate wave steepness (Hπ/L) in the cross-shore direction.

wave heights involves the steepening of the forced waves and the cell aspect ratio (1:4) selected for the simulation.

When the sinusoidal wave is forced at the offshore boundary it has an approximate steepness of 1:6, which is well below the cell aspect ratio of 1:4. As these waves shoal they become nonlinear and the face of the wave steepens quickly and dramatically within the first few meters of the cross-shore domain, as seen in Fig. 4–2. This steepening presents a problem when the slope of the free surface reaches or nears the cell aspect ratio, as the modified free surface velocity boundary conditions begin to translate momentum down the face of the wave a bit sooner than necessary to match the lab data. One result of this momentum transfer appears to be a reduction in the predicted wave heights. We say that the steepness ratios, shown in Fig. 4–2, are

approximate because we assume that the waveform is sinusoidal when we calculate the slope of the wave face. The modeled nonlinear waves exhibit surface slopes that exceed those calculated by our sinusoidal approximation.

One particular advantage of employing SOLA-SURF to simulate nearshore processes lies in its time-dependency. While steady-state wave models assume that wave shoaling is a stationary process, time-dependent processes such as the generation of a longshore current and undertow can affect wave transformation over time. Shown in Fig. 4–3, the RMS wave heights predicted by SOLA-SURF do not remain constant throughout the simulation. This suggests that the wave field responds continuously to the developing undertow and longshore current. These RMS values were calculated from a ten-wave average, centered about the simulation time shown in the legend.

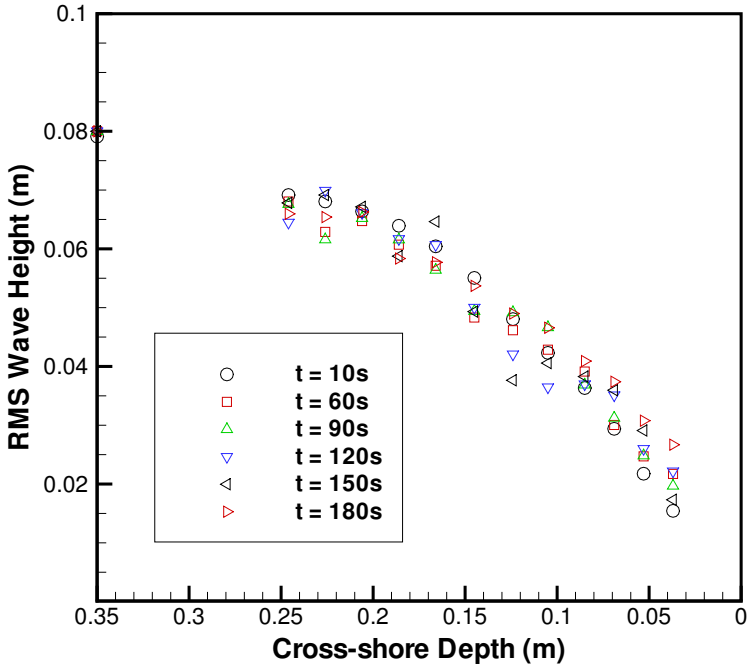

Figure 4–3: Statistical properties of the wave field at various time levels suggest that the wave shoaling in this experiment is not a stationary process.

4.1.2 Longshore Current Formation

The formation of the longshore current and the magnitude of the current velocities is highly sensitive to the implementation of the free surface velocity boundary conditions, as discussed above. Using the improved velocity boundary conditions provides reasonable estimates of the longshore current velocities, but fails to accurately predict the cross-shore wave heights. Our predicted current is calculated by first taking the depth and longshore averages of the longshore velocity component (w) and then by averaging these values over 30 wave-periods.[1]

As demonstrated by Fig. 4–4, the model approximately predicts the correct magnitude of the maximum longshore current velocity, but the peak is shifted shoreward of the location observed in the laboratory. This is perhaps due to the absence of setup at the shoreline owing to our choice of a shallow sill as an onshore boundary instead of an intersecting profile. Another feature of the predicted longshore current that was not observed in the laboratory experiment is the additional longshore-directed flow seaward of the peak velocity. This may be explained by referring to the predicted wave heights shown in Fig. 4–1. Underestimating the RMS wave height suggests an overestimation of the energy dissipation (Chen *et al.*, 2003), which manifests itself in the offshore region as additional longshore current velocity. The laboratory wave heights, on the contrary, remain somewhat constant until they near the point of breaking resulting in less longshore current velocity in the offshore region.

Apparently, other horizontal mixing processes in the lab experiment are not sufficiently strong to spread the mean longshore current significantly offshore of the breakpoint. In fact, the opportunity for longshore flow to persist in the offshore

[1] Henceforth, we denote depth-averaged values with a single overbar ($\bar{\ }$), depth and longshore-averaged values with two overbars ($\bar{\bar{\ }}$), and time-averaged values with the angle brackets ($\langle\ \rangle$).

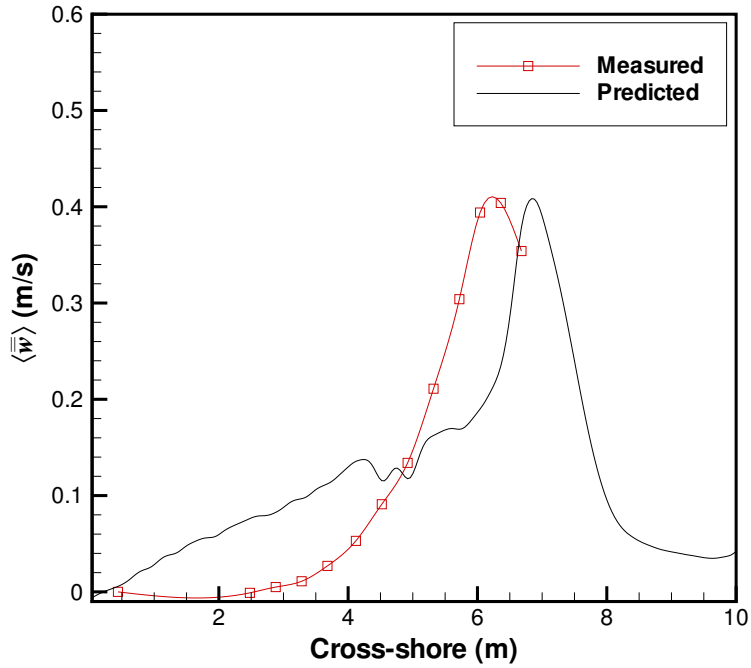

Figure 4–4: The predicted and measured longshore current velocities. A comparison of the predicted time-mean, depth and longshore-averaged, longshore current velocity to the measured current velocity. The predicted current is calculated at each cross-shore grid location and is represented here by the black line. The red line is a spline fit to Visser's data collection points, which are shown by the red squares.

region may be suppressed by the wave-guiding walls located at both ends of Visser's wave tank. These walls extend from above the mean water level to the bed, thus restricting any mean, longshore-directed flow between them. In a series of experiments of longshore currents on planar slopes, Galvin and Eagleson (1965) and Mizuguchi and Horikawa (1978) measured significant longshore velocities (20 to 40% of the maximum) seaward of the surfzone. These experiments were performed in similar wave tanks that provided clearance between the bed and the bottom of the wave guide and the results suggest that this configuration permits recirculation in the offshore region, where it was suppressed in Visser's experiment.

We allowed simulations to run for 200 seconds of model time, by which point the flow field had reached steady-state. In Fig. 4–5 we see the formation and growth

of the predicted average longshore current. Formation of the longshore current begins well seaward of the location of the predicted peak velocity and spreads laterally across the domain over time. After approximately 150 seconds of model time, the longshore current has reached steady-state: the magnitude and shape of the current vary little during the remainder of the simulation. Simulations were also run with two different sill depths to ensure that its location did not determine where the peak longshore velocity occurred. Sill depths of 1 cm and 2 cm were used in these simulations and the resulting average longshore currents are shown in Fig. 4–6. Regardless of the depth used, the maximum longshore current velocity remains in the same location, seaward of the sill, where the mean water depth is approximately 3 cm. The longshore current forms more slowly for the sill depth of 2 cm as compared to the depth of 1 cm, but this outcome was expected as twice as much volume is permitted to cross the sill.

4.2 Three-Dimensional Flow Features

4.2.1 Free Surface Visualizations

Normally incident waves propagating over longshore-uniform bathymetry produce circulation and flow features that are characteristically two-dimensional. Longshore gradients in velocity fields and wave heights resulting from obliquely incident waves, however, produce three-dimensional flow features in the nearshore region. One such feature is demonstrated by the longshore non-uniformities in the waves as they travel over a shearing current. Figure 4–7 contrasts the incident wave field from our simulation at an early time, when the undertow and longshore currents are undeveloped, and at a later time when both currents have reached steady-state. The incident wave field in Fig. 4–7A demonstrates the shoaling and refraction of the waves over the sloping bathymetry used in the laboratory experiment. The color contours in Figs. 4–7A and 4–7B correspond to the location of the free surface in the vertical domain, referenced to the still water level at $y = 0.35$ m. At this early time, when the currents have yet to develop, we see that the wave crests are more or less parallel to

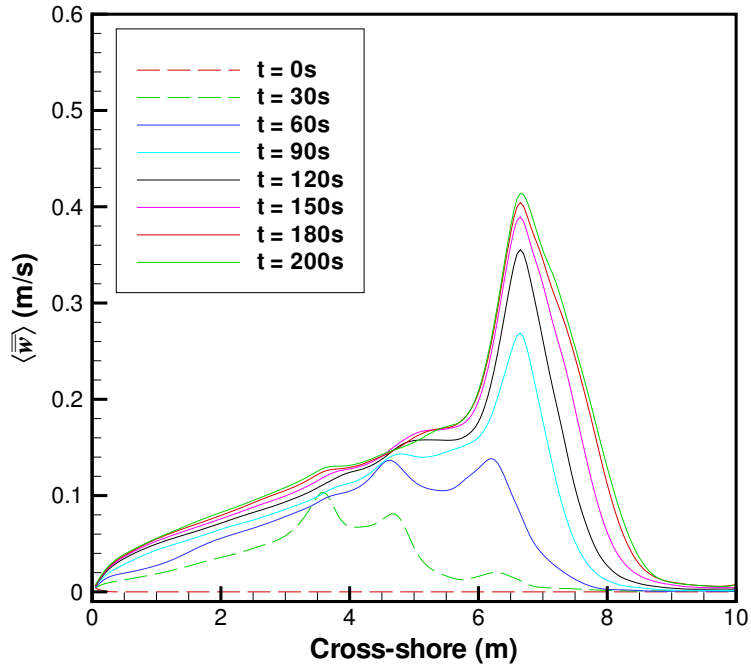

Figure 4–5: Time evolution of the average longshore current. Shown here are the depth and longshore-averaged, longshore current velocities taken at various times throughout the simulation. These profiles were averaged over ten wave-periods, centered around the time labels shown in the legend, to remove the wave component of the longshore velocity.

one another as they travel across the domain and that the periodic boundary conditions perform properly. The contrasting wave field shown in Fig. 4–7B, taken when the model has reached steady-state, shows the response of the wave field to the developed undertow and longshore currents. The relatively undisturbed, straight wave crests seen in Fig. 4–7A are now only found near the offshore boundary and those propagating over the shearing currents have significant longshore non-uniformities. Clearly, the incident waves begin to feel the mean currents for $x > 3$ m and produce spatially dependent wave breaking patterns.

4.2.2 Depth-Dependent Wave-Current Interaction

The three-dimensional nature of SOLA-SURF is perhaps even more useful for analyzing the depth-dependent circulations that develop in a complex flow field.

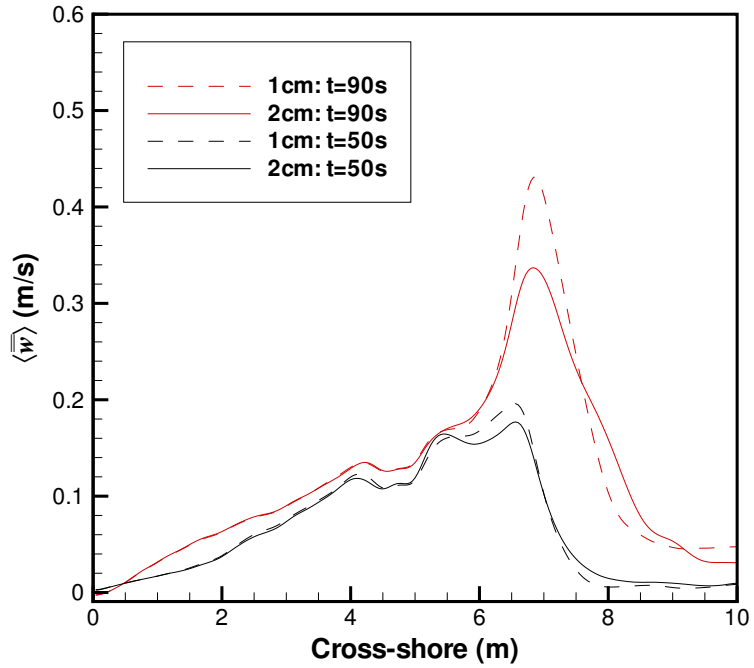

Figure 4–6: Average longshore current velocities over different sill depths. These profiles were averaged over ten wave-periods, centered around the time labels shown in the legend, to remove the wave component of the longshore velocity.

Vertical variations of the combined cross-shore and longshore current velocities were investigated by Svendsen and Lorenz (1989) and were said to have significant effects on the direction of sediment transport in the nearshore region. While many numerical investigations regarding undertow and longshore current velocity profiles have made use of depth-integrated or depth-averaged equations, the momentum equations used in SOLA-SURF explicitly include depth-dependent terms. The depth-dependent nature of the velocity field and cross-shore current is demonstrated by Fig. 4–8, where plots at two different times compare the developing velocity field at an early time with the fully developed field that occurs later in the simulation. The larger frames in Figs. 4–8A and 4–8B show the velocity field taken at every second cross-shore grid point, where the velocity vector is the resultant of the u and v velocity components. The area enclosed by the dark, black line in each frame corresponds to the area plotted in the smaller

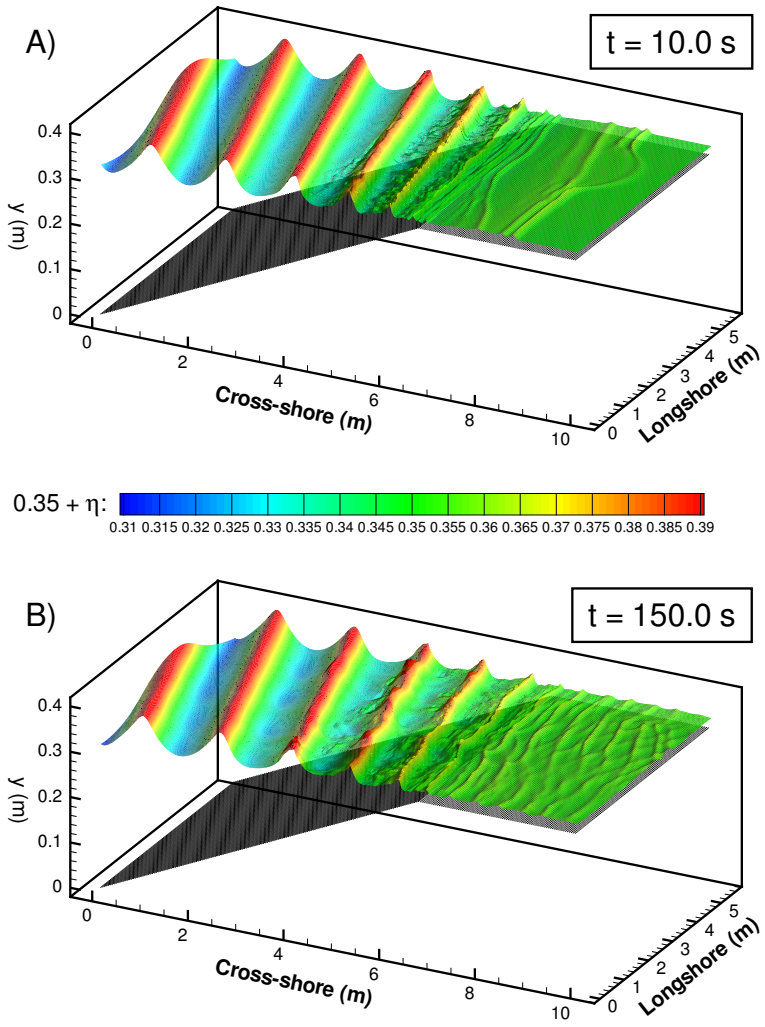

Figure 4–7: Three-dimensional visualizations of the instantaneous free surface. The contrasting wave fields show the effect of the shearing current on the incident wave field, taken at A) $t = 10$ s and at B) $t = 150$ s.

inset frames, where the velocity vectors are plotted at every computational grid cell. These instantaneous figures of the (x, y) plane are transects taken from the middle of the longshore domain. Figure 4–8A shows the depth-dependent velocity field resulting from the incident wave field where, demonstrated by the color contour plot of u in the panel inset, the undertow has yet to develop. In Fig. 4–8B, however, the undertow is fully developed and the resulting velocity field is now much more complicated, as

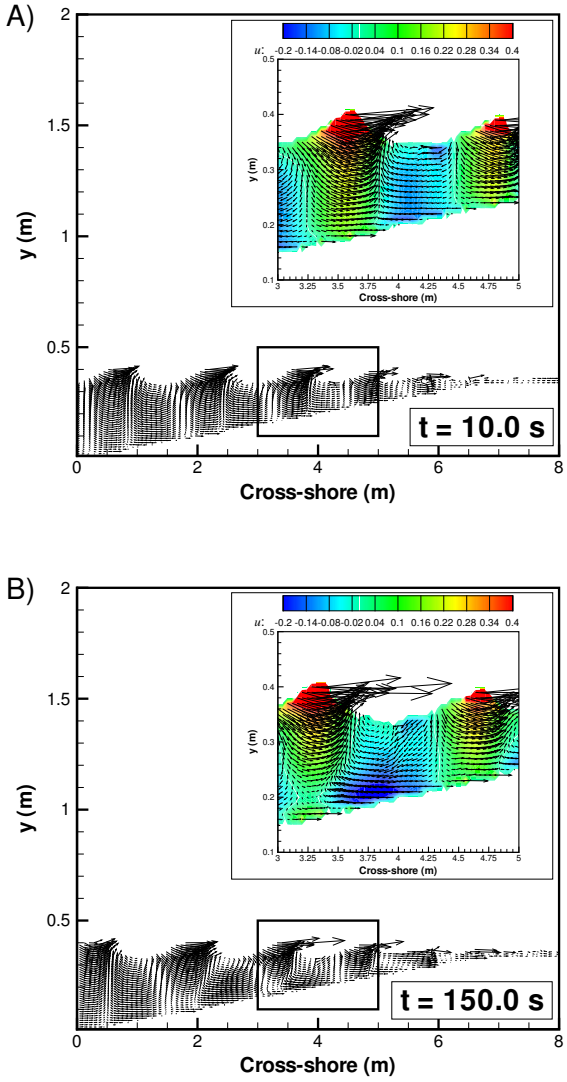

Figure 4–8: Depth-dependent wave-current interactions in the cross-shore. Velocity fields taken at A) $t = 10$ s and at B) $t = 150$ s show the depth-dependent velocity predictions and the superposition of a propagating wave on the developed undertow.

shown by both the inset panel and the larger frame. At this later time, the incident waves are propagating across a lower-frequency, seaward-directed flow near the bed that is of similar magnitude to the shoreward-directed velocities of the obliquely incident wave field. Note the increased strength of the velocity at the wave crest in the inset of Fig. 4–8B and the resulting shear in the velocity field under the wave crest.

4.2.3 Longshore Current Variability

While not discussed in Visser (1991), the time-dependent longshore current predicted by SOLA-SURF is also spatially variable in both horizontal directions. This time-dependent current structure is shown in panels A, B, and C of Fig. 4–9, where we have plotted the instantaneous, depth-averaged $(\overline{u}, \overline{w})$ velocity field in the (x, z) plane at three times during the simulation. The velocity field shown in Fig. 4–9D represents a thirty second average, centered about $t = 165$ s, of the depth-averaged $(\overline{u}, \overline{w})$ velocities taken once the model had reached steady-state. For clarity, every fifth velocity vector in the longshore direction is plotted in this figure but none have been omitted from the cross-shore direction. In Fig. 4–9A, at $t = 20$ s, we see that the predominant feature of the velocity field is the incident wave signal and note that, relative to the onshore-directed velocities, the velocity magnitudes of reflected waves on the sill are very small. At roughly half of the time it takes the longshore current to reach steady-state, there appears to be a longshore-periodic structure associated with the longshore current, which is shown in Fig. 4–9B. Figure 4–9C demonstrates the persistence of this meandering periodic structure, although much weaker, even as the mean longshore current nears steady-state. The thirty second average of the depth-averaged, steady-state velocity field shown in Fig. 4–9D removes the velocity signature of the incident wave field, resulting in a mostly longshore uniform current.

Further investigation of the periodic structure associated with the developing longshore current (Fig. 4–9B) suggests that oscillations of the current occur in both the longshore and cross-shore directions. Over a thirty second period spanning from $t = 90$ s to $t = 120$ s, when the mean current speed and profile are evolving, the depth-averaged longshore velocity is not uniform in the longshore direction. The periodic structure shown in Fig. 4–10A represents the time-mean, depth-averaged longshore current for $90 < t < 120$ s and shows that this feature oscillates with a much lower frequency than the incident wave field: on the order of twenty seconds.

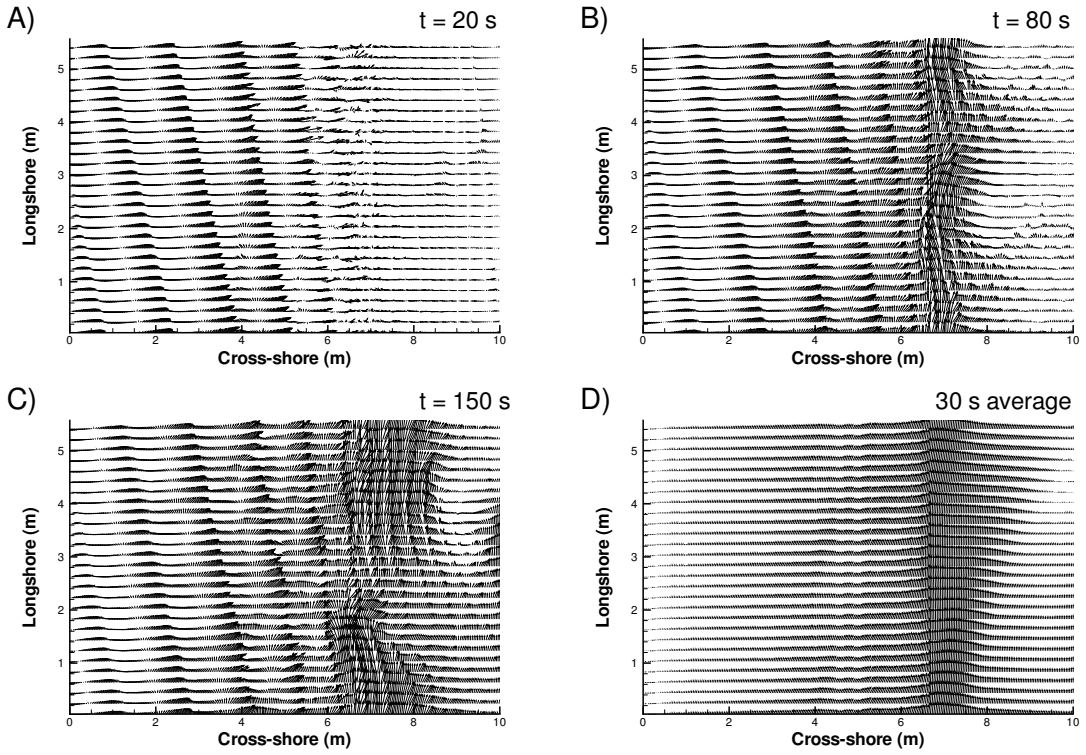

Figure 4–9: Depth-averaged $(\overline{u}, \overline{w})$ velocity fields taken at A) $t = 20$ s, B) $t = 80$ s, C) $t = 150$ s, and D) over a 30 second average to remove the effects of the incident wave field. Note the longshore variability of the current structure in panels B and C.

Nearshore motions with frequencies of this magnitude are often classified as shear waves, but the presence of these motions were not discussed in Visser (1984) or Visser (1991). Panels B and C of Fig. 4–10 are color contour plots of the instantaneous, depth-averaged residual longshore velocity at $t = 100$ s and $t = 120$ s respectively. The residual velocity component is found using a Reynolds decomposition (Pope, 2000) for the depth-averaged velocity and is given by Eq. 4–1. Here, the residual longshore velocity considered accounts for the wave-induced velocity as well as the turbulence, but no distinction is made between the two components.

$$\overline{w}' = \overline{w} - \langle \overline{w} \rangle \tag{4–1}$$

Alternating velocity deficit (blue) and velocity excess (red) signatures seen in Figs. 4–10B and 4–10C demonstrate the longshore propagation of this instability,

as well as its cross-shore displacement. As compared to the residual velocity signatures shown in Fig. 4–10B, notice that the excess and deficit signatures have reversed their positions in the longshore direction and have migrated seaward in Fig. 4–10C.

Shear waves are energetic, low-frequency vortical structures that propagate in the longshore direction and exhibit significant excursions in the horizontal plane (Bowen and Holman, 1989). Thus, these shear wave motions contribute greatly to the nearshore

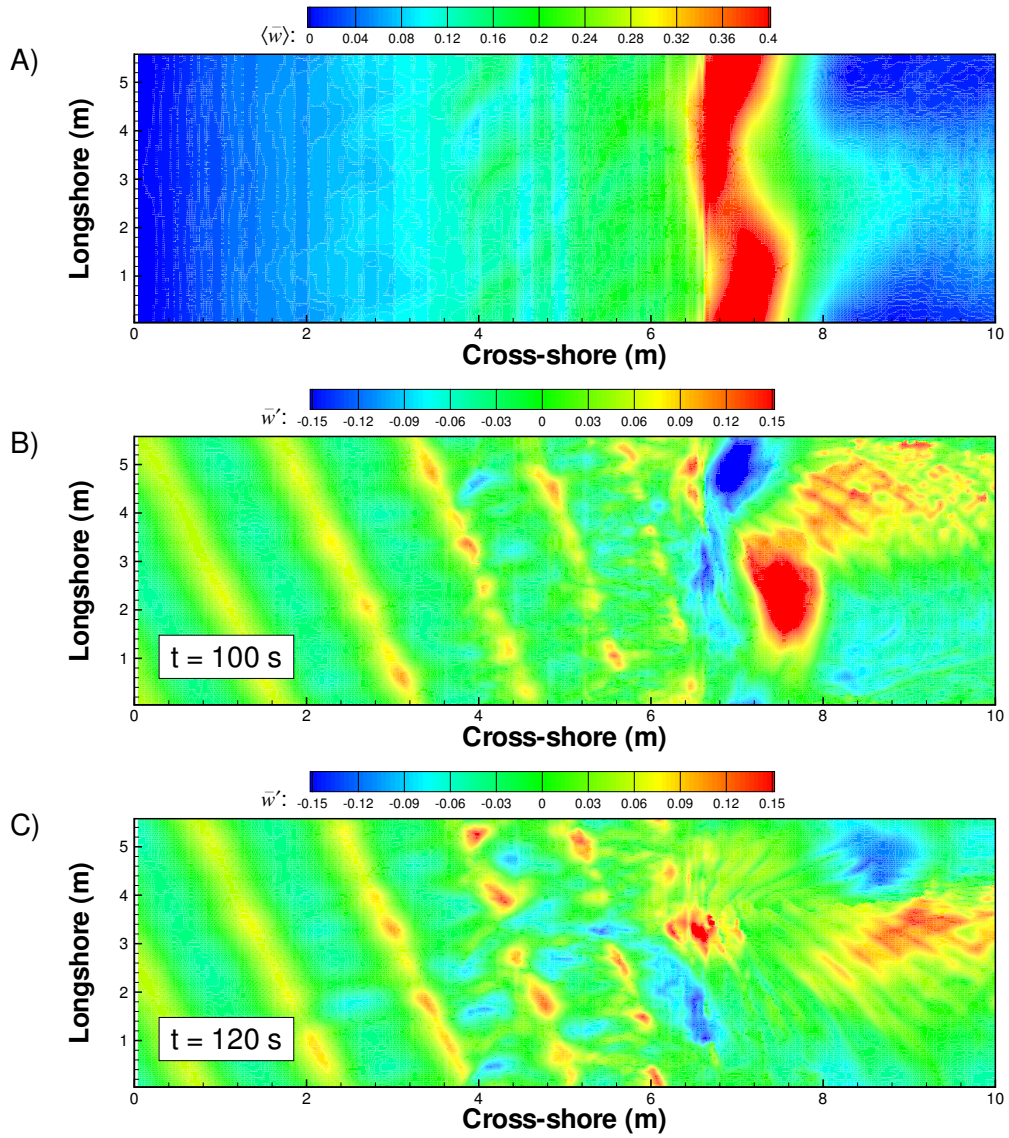

Figure 4–10: Color contour plots of the depth-averaged longshore velocity for A) a 30 s time-period prior to steady-state, B) the instantaneous longshore velocity residual at $t = 100$ s and C) the instantaneous longshore velocity residual at $t = 120$ s.

circulation and ultimately affect the transport of sediment, pollutants, and biological material (Dodd *et al.*, 2000). While barred beaches have been found to facilitate the onset of shear instabilities [see Oltman-Shay *et al.* (1989); Bowen and Holman (1989)], observations of these motions on planar beaches are not widespread but have been known to occur (Dodd *et al.*, 2000). Oltman-Shay and Howd (1993) discovered evidence of shear wave motions on two planar beaches in California (Leadbetter Beach and Torry Pines) after reanalyzing data from the Nearshore Sediment Transport Study (NSTS) conducted in 1980. Shear waves have not been readily identified in laboratory experiments conducted with planar slopes (Reniers *et al.*, 1997) either because of limitations in data collecting or due to suppression by confinement of the wave basin (Bowen and Holman, 1989). In their numerical model, Allen *et al.* (1996) were successful in generating shear waves over a planar beach and Putrevu and Svendsen (1992) suggested that typical length and time-scales of shear wave motions from the experiments of Visser (1984), if they had been identified, would be of *O*(8 m) and *O*(20 s), respectively. These scales agree well with those predicted by the simulation ($\sim$20 s and $\sim$5.6 m), resulting in a phase speed of roughly 70% of the maximum longshore current velocity—similar to the value suggested by Dodd *et al.* (2000).

4.3 Vertical Distributions of Velocity and Momentum

4.3.1 Time-Averaged Velocity Profiles

Although the cross-shore circulation was not discussed in Visser (1991), time-averaged velocity profiles of the predicted flow field show a strong seaward-directed flow near the bed, commonly referred to as undertow. The velocity profiles plotted in Fig. 4–11 demonstrate this behavior of the return flow, specifically in panels B, C, and D, where the undertow dominates the circulation. Velocity profiles shown in Fig. 4–11 were averaged over thirty seconds and were taken from a transect located near the mid-point of the longshore domain. The slightly negative u and w velocity profiles in Fig. 4–11A result from the velocity corrections applied at the forcing boundary

that account for mass flux. Figure 4–11A also demonstrates that, as expected, there is a shoreward-directed flux of momentum due to the waves that roughly occupies the region bound by the wave trough and wave crest. While this momentum flux due to the waves persists throughout the remaining panels, the vertical structure of the velocities change significantly as the locations progress from the forcing boundary shoreward.

The time-averaged longshore velocity profiles in Figs. 4–11B and C demonstrate a unique behavior near the two grid points closest to the bed. Here, the time-averaged longshore current receives an asymmetric impulse from the staircase representation of the bottom slope. As the shoreward velocity of the phase of a shoaling wave encounters a step rise, there is a corresponding pulse of near-bottom water that flows in the positive z-direction since the fluid is less likely to flow upward due to the mass above it. Similarly, for the seaward-directed velocity of the opposing phase there is a pulse of water in the negative z-direction.

The magnitude of the undertow diminishes significantly in the locations where the longshore current velocities are high, as demonstrated in panels E through H of Fig. 4–11. The predicted distribution of longshore velocity is similar, in most profiles, to the nearly depth-uniform structure reported by Visser (1991) and discussed by Svendsen and Lorenz (1989), who suggested that a depth-uniform velocity profile would be a better assumption than the logarithmic profiles more commonly used to describe steady, open-channel flows. This depth-uniform structure is most evident in the strongest (higher velocity) part of the longshore current and is demonstrated by Figs. 4–11G and 4–11H. Figure 4–11 also shows the large difference between the magnitudes of the horizontal velocities, u and w, and the vertical velocity v, which is so small that you can barely distinguish it in the figure. This implies that the average vertical velocity contributes very little to the mean flow and becomes even less significant if considered in a depth-averaged or depth-integrated sense. Products of the

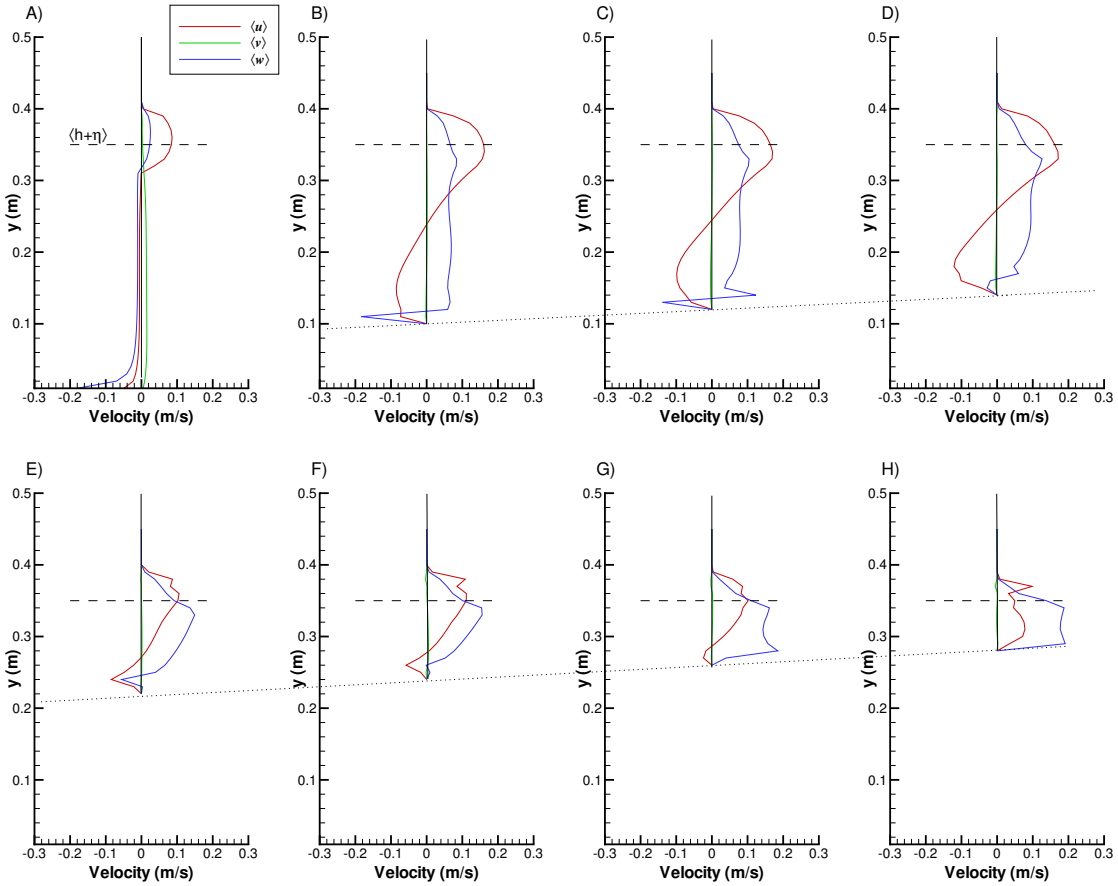

Figure 4–11: Time-averaged velocity profiles at A) the forcing boundary, B) $h = 0.246$ m, C) $h = 0.226$ m, D) $h = 0.206$ m, E) $h = 0.145$ m, F) $h = 0.124$ m, G) $h = 0.085$ m, and H) $h = 0.069$ m. The dashed line in each panel represents the mean water level while the dotted line shows the approximate location of the bottom boundary. These panels represent a progression from the offshore forcing boundary (A) to the shallow depths of the inshore (H) where the longshore current dominates the nearshore circulation.

vertical velocity with horizontal velocity components, however, may not necessarily be insignificant in the presence of a nonlinear, propagating wave field.

Time-mean velocity profiles of u in panels B, C, and D of Fig. 4–11 suggest that the conservation of mass is being satisfied as depth-averaged values of the profiles are very close to zero. This is not the case in panels E through H, where there appears to be a net flow of mass in the shoreward direction. However, the shoreward-directed momentum carried by the incident wave field is balanced by the undertow only in

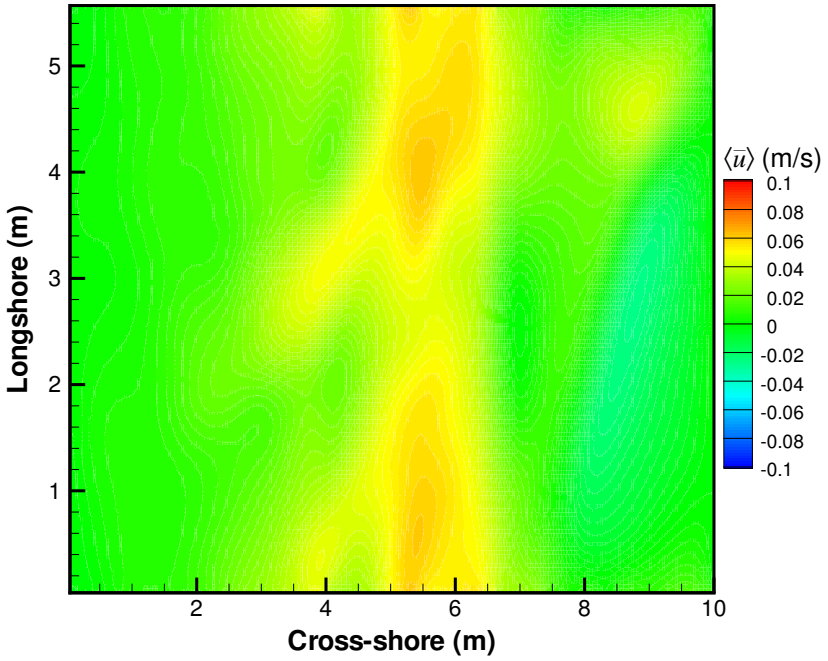

Figure 4–12: The depth-averaged cross-shore velocity, u, averaged over thirty seconds and plotted in the (x, z) plane.

a strictly two-dimensional sense (Svendsen, 1984); previous figures and discussions have emphasized the three-dimensionality of the flow field. A color contour plot of the time-mean, depth-averaged cross-shore velocity is shown in Fig. 4–12 where hotter colors correspond to shoreward-directed flow and cooler colors designate seaward-directed flow. The concentration of shoreward-directed flow between $x = 5$ m and $x = 6.5$ m corresponds to the area where the velocity profiles in panels E–H of Fig. 4–11 are located. The depth-averaged cross-shore velocity was averaged over a thirty second period just prior to reaching steady-state, during which time there were many complex, spatial and time-dependent flow features including seiching and the periodic oscillations of the longshore current. These different flow features all occur on different length and time scales making it difficult to extract an ensemble that explicitly proves that the depth-averaged velocity profiles obey the conservation of mass. We

know, however, that the model conserves mass over the course of a 200 second simulation: the initial volume of fluid contained within the physical domain is the same as the volume contained at the end of the simulation. Another significant feature of this region is the setup, and the location of the time-mean free surface displacement seems to correspond well with the location of the excess shoreward-directed velocity. Additional information about the spatial relationship between these two features is presented in Appendix B.

4.3.2 Vertical Distribution of Radiation Stress

The vertical distributions of the shoreward-directed components of the radiation stress have received particular attention recently [Mellor (2003), Xia *et al.* (2004)]. As presented in Longuet-Higgins and Stewart (1964), these two horizontal components are the cross-shore component of the shoreward-directed radiation stress and the longshore component of the shoreward-directed radiation stress, denoted here as S_{xx} and S_{xz},[2] respectively, and are given by Eqs. 4–2 and 4–3. The longshore component of the shoreward-directed radiation stress is non-zero only for a three-dimensional wave climate produced by either obliquely incident waves or longshore variable bathymetry. We have neglected a third horizontal radiation stress component, S_{zz}—the longshore-directed component—for two reasons: first, the vertical structure of the time-averaged longshore flow is essentially depth-uniform and, as such, vertical distributions would not be as complex as those in the cross-shore and, second, since longshore gradients of the time-averaged quantities that contribute to this stress component would be zero owing to our periodic longshore domain. Following Longuet-Higgins and Stewart (1964), we define:

[2] Although the notation of S_{xy}, presented by Longuet-Higgins and Stewart, is more commonly used, we shall use this alternative notation since it is consistent with our coordinate system.

$$S_{xx} = \left\langle \int_{-h}^{\zeta} (p + \rho u^2)\, dy \right\rangle - \int_{-h}^{0} p_0\, dy \tag{4–2}$$

$$S_{xz} = \left\langle \int_{-h}^{\zeta} \rho u w\, dy \right\rangle \tag{4–3}$$

where
$h =$ bed elevation
$\zeta =$ vertical location of the free surface
$\rho =$ density of the fluid
$p =$ total pressure
$p_0 =$ hydrostatic pressure in the absence of waves
$\langle \quad \rangle =$ time-averaging operator

In order to obtain information regarding the vertical structure of the radiation stress components, we simply neglect the vertical integration of the expressions presented in Eqs. 4–2 and 4–3 and denote the depth-dependent values of the radiation stress components by s_{xx} and s_{xz}. The resulting equations for the shoreward component of the shoreward-directed radiation stress and the longshore component of the shoreward-directed radiation stress are given by Eqs. 4–4 and 4–5, respectively,

$$s_{xx}(y) = \rho\langle u^2 \rangle + \langle p \rangle - p_0 \tag{4–4}$$

$$s_{xz}(y) = \rho\langle uw \rangle \tag{4–5}$$

The formulation of Eq. 4–4 is much easier to understand when evaluating the vertical structure of each component and their relative magnitudes. Figure 4–13 shows the distribution and magnitude of each component of s_{xx}, as well as the total, where values have been averaged over thirty seconds. Instead of plotting both pressure components, the difference between the two is shown in order to reduce the scale of the abscissa and increase the resolution of each component. Note that the units of s_{xx} shown on the abscissa characterize a stress, while depth-integrated values of the radiation stress terms (S_{xx} and S_{xz}) have the units of stress times length. The dashed

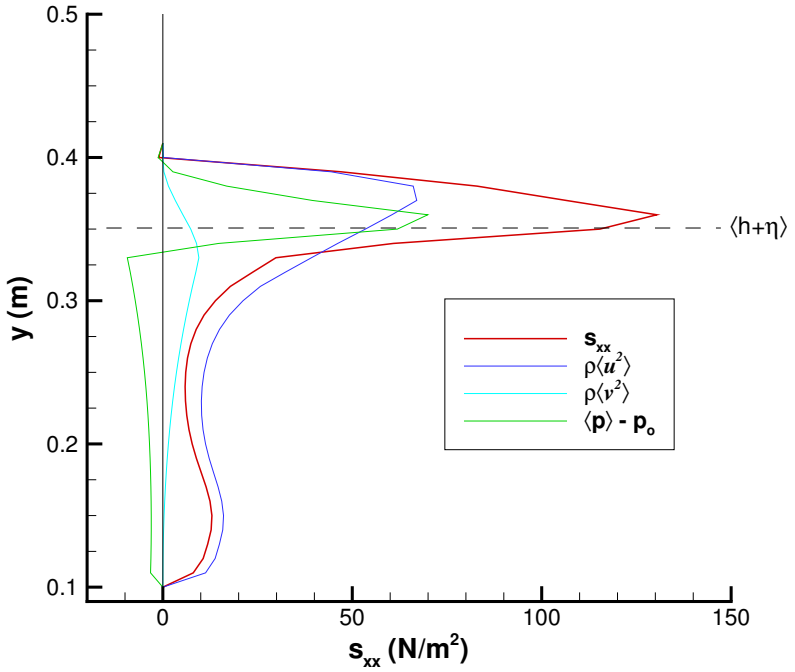

Figure 4–13: A comparison of the shape and magnitude of various components of s_{xx} taken from a location in the middle of the longshore domain where the local depth is $h = 0.246$ m.

line in Fig. 4–13 represents the mean water level over the thirty second average at a location where the mean water depth is 0.246 m and the location of the bed is at $y = 0.104$ m.

The total pressure term in Eqs. 4–2 and 4–4 is the time-mean pressure in the progressive wave field and, thus, represents both the pressure due to the water waves as well as the hydrostatic pressure over the water column. Plotting the difference between the time-mean total pressure and the hydrostatic pressure in the absence of a wave field (Fig. 4–13) results in the time-mean dynamic pressure due to the incident waves. Between the trough and crest levels, Fig. 4–13 shows that the apparent stress term ($\rho\langle u^2\rangle$) and the gravitational term ($\langle p\rangle - p_0$) contribute approximately equal amounts of momentum flux. This is in contrast to the findings of Sobey and Thieke (1989) who stated that the gravitational term was dominant above trough level and that the apparent

stress was less significant in this region; however, the magnitude of the wave apparent stress above the trough is roughly five-times greater than the predicted value in the undertow, which is similar to their findings. While nonlinear cnoidal theory was used in their investigation, the waves predicted in this model are strongly nonlinear, which is evident in the translation of the apparent stress peak above the mean water level.

The expression $\rho\langle v^2\rangle$, while not included in our formulation of s_{xx} (Eq. 4–4), is also included in Fig. 4–13 to demonstrate its relative significance to the other terms. More specifically, it shows that there is not an exact balance between the vertical flux of momentum ($\rho\langle v^2\rangle$) and the time-mean dynamic pressure ($\langle p\rangle - p_0$) below the mean water level (the difference in sign, however, is correct). This contradicts the methodology followed by Longuet-Higgins and Stewart (1964) in their formulation of the radiation stress equation for S_{xx}, where the terms were considered to explicitly balance one another below the mean water level. A formulation for s_{xx} suggested by Sobey and Thieke (1989) accounted for this inequity:

$$s_{xx}(y) = \rho\langle u^2\rangle - \rho\langle v^2\rangle + \Delta p, \tag{4–6}$$

where we have adapted our notation for the time-averaging and accounted for the difference in the coordinate systems by replacing w^2 with v^2. Here the pressure term Δp accounts for the time-average dynamic pressure in the region bound by the wave crest and wave trough; therefore, the vertical momentum flux term $\rho\langle v^2\rangle$ is assumed to exactly balance the time-average dynamic pressure below the trough level. As shown in Fig. 4–13, the shape and magnitude of the profiles corresponding to the terms in question are not similar, especially near the bed where the momentum tends toward zero much faster than the dynamic pressure.

Using the formulation for s_{xx} given by Eq. 4–4, we have plotted the predicted profiles of the shoreward-directed radiation stress, along with the analytical solution provided by Longuet-Higgins and Stewart (1964) (Eq. 4–7) for the linear distribution

of the total energy (E), a triangular distribution of $\frac{\mathrm{E}}{2}$ (Eq. 4–8) above the mean trough level (Dean, 1995), and the vertical distribution of s_{xx} suggested by Mellor (2003) (Eq. 4–9).

$$S_{xx} = E\left(\frac{2hk_x}{\sinh 2hk_x} + \frac{1}{2}\right) \tag{4–7}$$

$$s_{xx}(y) = \frac{\rho g H \cos\theta}{2\pi}\left[\sqrt{1-\left(\frac{2y}{H}\right)^2} - \frac{2y}{H}\cos^{-1}\left(\frac{2y}{H}\right)\right] + \begin{cases} 0 & \text{if } y > \text{MWL} \\ \rho g y & \text{if } y < \text{MWL} \end{cases} \tag{4–8}$$

$$s_{xx}(y) = kDE\left[F_{12}F_{11}\left(\frac{k_x^2}{k^2}+1\right) - F_{22}F_{12}\right] \tag{4–9}$$

where

$$F_{11} = \frac{\cosh kD(1+\upsilon)}{\cosh kD} \quad F_{12} = \frac{\cosh kD(1+\upsilon)}{\sinh kD} \quad F_{22} = \frac{\sinh kD(1+\upsilon)}{\sinh kD}$$

$\upsilon =$ transformed vertical coordinate such that $\upsilon = \begin{cases} -1 & \text{if } y = -h \\ 0 & \text{if } y = \zeta \end{cases}$

and
$E =$ total wave energy = $\frac{1}{8}\rho g H^2$
$h =$ local water depth
$\theta =$ local wave angle
$D = h + \langle\eta\rangle$
MWL = mean water level

The profile of s_{xx} predicted by SOLA-SURF in Fig. 4–14A approximates a depth-uniform profile since there is essentially no mean-flow below the trough level at the offshore forcing boundary. This location is of particular interest because the predicted profile is representative of the radiation stress produced by the time-averaged wave forcing. At the forcing boundary, the predicted profile agrees well with the distribution of momentum given by linear theory since the forced waves are sinusoidal and approximately linear. The magnitudes of the triangular and depth-uniform segments would be larger had we not applied corrections to the forcing velocities to account for mass flux. Although the waves are forced with a linear, sinusoidal-type

signal, they steepen and become asymmetric as they shoal, dramatically affecting the distribution of momentum flux.

The predicted profiles of s_{xx} (Fig. 4–14) between the trough and crest levels have a triangular-shaped distribution of momentum flux that accounts for the majority of the shoreward-directed flux, similar to observations made by Svendsen (1984) and Sobey and Thieke (1989). While the peaks of the predicted radiation stress profiles have magnitudes similar to those predicted by linear theory, the nonlinearity of the simulated waves redistributes the majority of the momentum above trough level and shifts the peak of the profile above the mean water level. The predicted time-average circulation gives the radiation stress profile a very distinct shape below the trough level, especially in Figs. 4–14B–D where the undertow is the dominant flow feature. Progressing up the slope of the bathymetry, in Figs. 4–14E–H, we see that the mean flow is relatively depth-uniform, below the trough level, in the locations where the longshore current velocities are highest; however, the average magnitude of the profiles below the trough level vary little throughout the cross-shore.

Mellor's equation for the vertically dependent shoreward-directed radiation stress (Eq. 4–9) provides an alternate approximation for the distribution of momentum. In some instances (Figs. 4–14E–H), the magnitude of the radiation stress near the bed is actually greater than the value at the crest level. One possible benefit of the analytical solution provided by Mellor (2003) is that it provides some level of approximation concerning the termination of the vertical distribution at the crest level while the linear distribution of momentum flux suggested by Longuet-Higgins and Stewart (1964) simply stops at the mean water level. Perhaps a suitable compromise between the analytical solution provided by linear theory and that provided by Mellor (2003) would be to add the triangular distribution of $\frac{\mathrm{E}}{2}$ to Mellor's profile, starting at the crest level. Neglecting the characteristics and vertical structure of the mean flow field, it is possible that a depth-uniform distribution of the radiation stress below trough level would

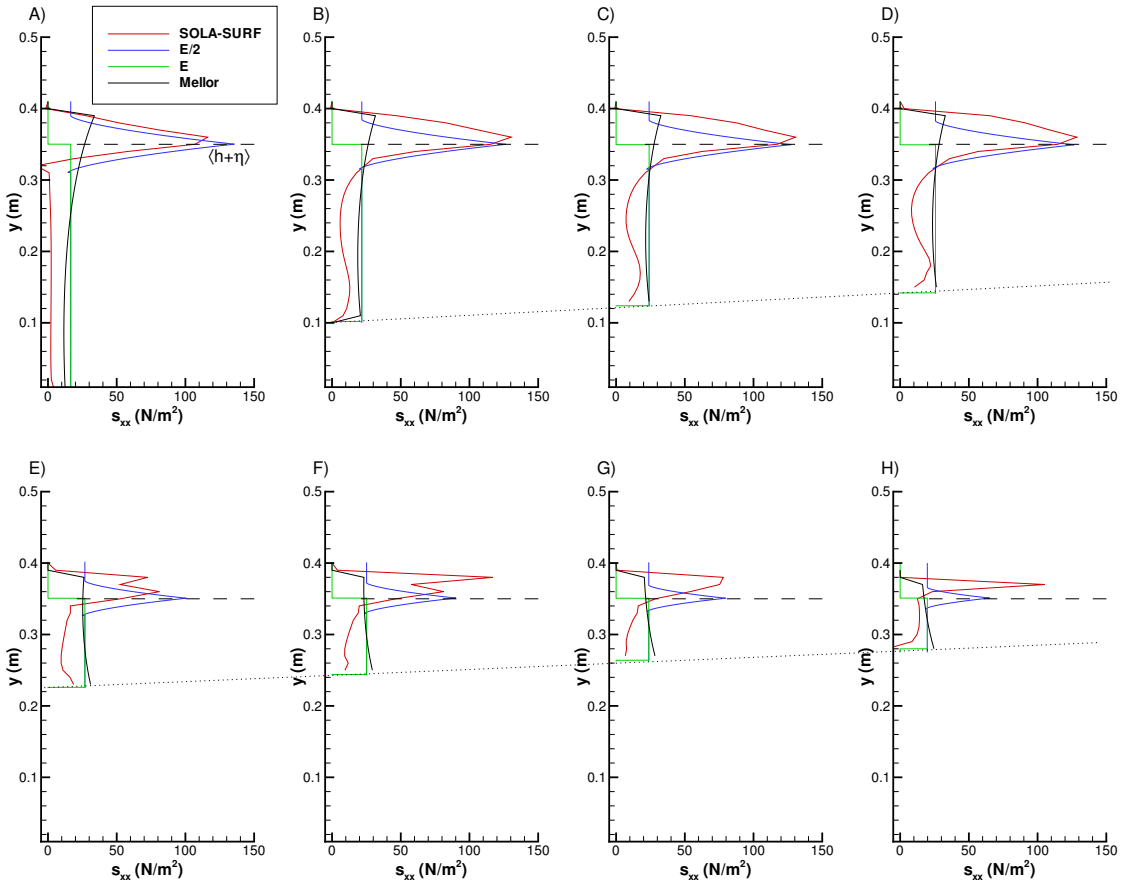

Figure 4–14: Predicted profiles of radiation stress s_{xx}. A comparison of the predicted shape and magnitude of s_{xx} to linear theory and Mellor's analytical solution at A) the forcing boundary, B) $h = 0.246$ m, C) $h = 0.226$ m, D) $h = 0.206$ m, E) $h = 0.145$ m, F) $h = 0.124$ m, G) $h = 0.085$ m, and H) $h = 0.069$ m. The triangular distribution of $\mathrm{E}/2$ has been shifted to the right for purposes of comparison. The dashed line represents the mean water level and the sloping, dotted line represents the approximate location of the bathymetry.

provide a sufficiently realistic representation of the momentum flux caused by the time-averaged wave forcing.

Vertical distributions of the longshore component of the shoreward-directed radiation stress, s_{xz}, are shown in Fig. 4–15 where the plotting convention is similar to that used in Fig. 4–14. The predicted profile of s_{xz} was plotted using the vertically-dependent formulation given by Eq. 4–5, which was derived from the depth-integrated equation (Eq. 4–3) suggested by Longuet-Higgins and Stewart

(1964). Figure 4–15 shows the comparison of the predicted radiation stress profile to the depth-uniform distribution of momentum flux (E) predicted by linear theory and suggested in Dean and Dalrymple (1991) (Eq. 4–10), and the vertical distribution proposed by Mellor (2003) (Eq. 4–11).

$$S_{xz} = \frac{E}{4}\left(\frac{2hk}{\sinh 2hk} + 1\right)\sin 2\theta \tag{4–10}$$

$$s_{xz}(y) = kDE\left[F_{12}F_{11}\left(\frac{k_x k_z}{k^2}\right)\right] \tag{4–11}$$

The modeled vertical profiles of s_{xz} above the trough level exhibit the triangular distribution seen in the s_{xx} profiles of Fig. 4–14, but the peak of the profile is shifted further above the mean water level. As shown in the radiation stress component profiles of Fig. 4–13, the gravitational term reduces the super-elevation of the peak of the s_{xx} profile. Since there are no additional terms in the formulation of the vertically-dependent profile of s_{xz}, the wave apparent stress term controls the shape of the profile and the distribution of momentum flux. This suggests that assuming similar distributions of s_{xx} and s_{xz} above trough level, and at different cross-shore positions, is inaccurate in the presence of propagating nonlinear water waves. Below trough level, however, the distribution of momentum is relatively depth-uniform with the exception of Figs. 4–15E and 4–15F where the seaward-directed undertow produces an inflection point near mid-depth.

Comparisons of the predicted profile of s_{xz} to the linear solution and the analytical solution given by Mellor (2003) give mixed results. Similar to the comparison of s_{xx} profiles in Fig. 4–14, Mellor's formulation (Eq. 4–11) dramatically under-predicts the magnitude of momentum distributed above the trough level but correctly estimates the upper-most extent of the distribution profile. At the two most offshore locations (panels A and B of Fig. 4–15), however, the distribution of momentum below the trough level given by Mellor's equation looks very similar in shape and magnitude to

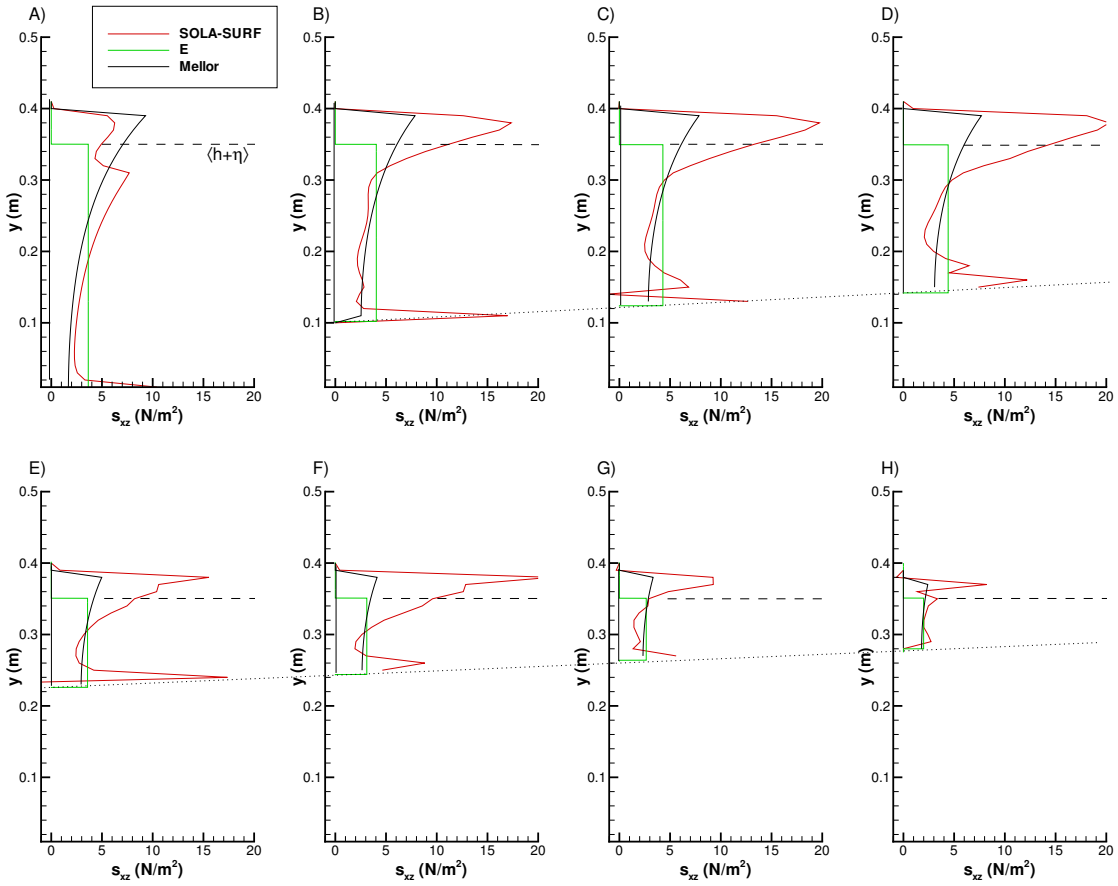

Figure 4–15: Predicted profiles of time-averaged radiation stress s_{xz}. A comparison of the predicted shape and magnitude of s_{xz} to linear theory and Mellor's analytical solution at A) the forcing boundary, B) $h = 0.246$ m, C) $h = 0.226$ m, D) $h = 0.206$ m, E) $h = 0.145$ m, F) $h = 0.124$ m, G) $h = 0.085$ m, and H) $h = 0.069$ m. The dashed line represents the mean water level and the sloping, dotted line represents the approximate location of the bathymetry.

both the predicted profile and the depth-uniform distribution suggested by linear theory. Moreover, Fig. 4–15A shows a very close agreement between Mellor's solution and the predicted profile at the forcing boundary.

The previous figures demonstrating the distribution of radiation stress (Figs. 4–14 and 4–15) show that the majority of the momentum flux is located above the trough level. Although the various methods for plotting vertical profiles of s_{xx} and s_{xz} give vastly different distributions over the vertical, their depth-integrated values are similar, which is an encouraging result. The depth-integrated radiation stress magnitudes

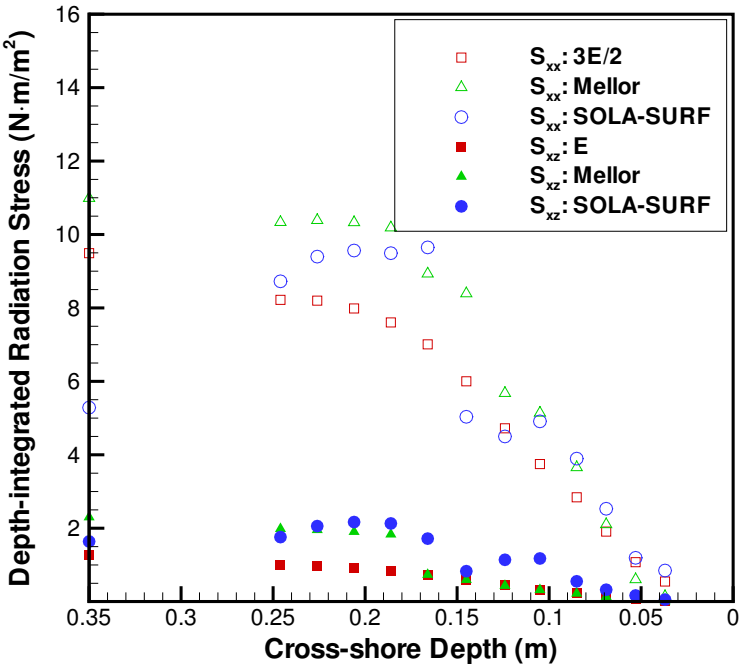

Figure 4–16: The depth-integrated magnitudes of the predicted radiation stresses (S_{xx} and S_{xz}) show good agreement to the magnitudes found from linear theory and Mellor's equations.

are shown in Fig. 4–16 and demonstrate the similarity of the predicted magnitude with that given by linear theory (E + $\frac{\mathrm{E}}{2}$) and Mellor's equations given previously. Depth-integrated values of the radiation stress component S_{xx} are represented by the hollow symbols where each shape represents the technique or theory given in the symbol legend. The longshore component of radiation stress S_{xz} is denoted by the filled symbols, which again correspond to the approximation listed in the legend.

A multiple-application trapezoidal scheme (Chapra and Canale, 1998) was used to integrate the vertically-dependent profiles plotted in Figs. 4–14 and 4–15, and at five additional cross-shore locations as well. With the exception of the values predicted at the forcing boundary, the predicted magnitudes of S_{xx} and S_{xz} look quite similar to the analytical solutions provided by the other two theories considered here. The forcing boundary presents a special case since corrections have been applied to the velocity

components to compensate for mass flux. As discussed earlier, and shown in Fig. 4–14, the velocity corrections applied at the forcing boundary result in a mean-flow field below the trough level that is just slightly larger than zero; therefore, the largest contribution to the depth-integrated value of S_{xx} comes from the momentum flux associated with the forced, monochromatic wave signal. This is not the case at other cross-shore locations where the undertow and longshore current contribute significantly to the structure and magnitude of the radiation stress profile below the trough level of the waves. Since we do not have a formulation for the triangular distribution of the radiation stress component s_{xz} between the wave crest and trough, the depth-integrated value of S_{xz} only includes the portion of the profile below the mean water level.

The distribution of the radiation stress produced by the nonlinear waves in our simulations suggests that the majority of the momentum flux is contained above the trough level. Similar observations were made by Svendsen (1984) and Sobey and Thieke (1989) regarding the shoreward-directed component of the radiation stress, S_{xx}. From the predicted profiles of the longshore component presented in Fig. 4–15, it appears that this observation holds true for S_{xz} as well. This distribution of energy over the water column is not a trivial matter as phase-averaged models may be forced with various approximations to stress or force distributions, a common choice being depth-uniform or depth-linear profiles. Linear theory suggests that roughly one-third of the total momentum flux is advected shoreward by the waves in the region between the trough and the crest. By integrating our radiation stress profiles of s_{xx} and s_{xz} and comparing the area contained in the region bound by the crest and the trough to the total area of the profile, we find rather that roughly twice this amount is carried by the nonlinear waves present in our simulations. This ratio is plotted in Fig. 4–17 for both S_{xx} and S_{xz}, where we have once again used the multiple-application rule to integrate the profiles.

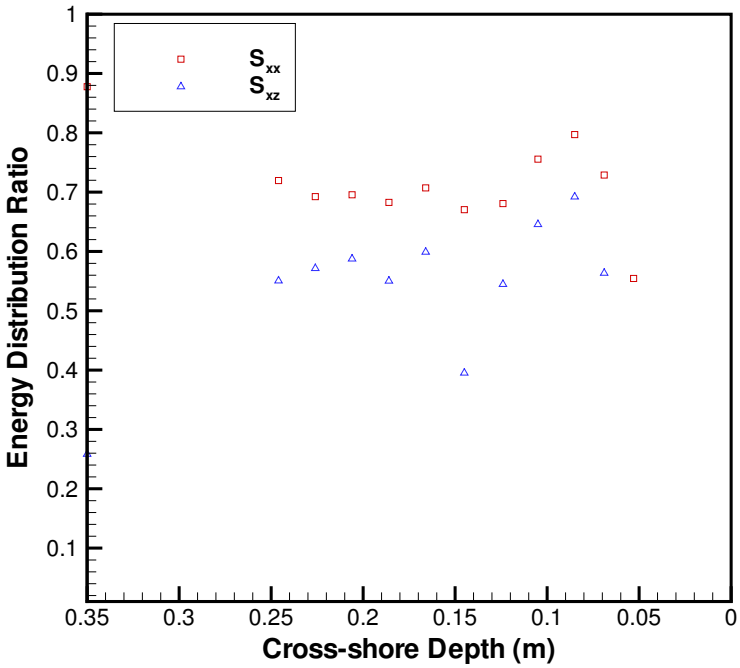

Figure 4–17: The ratio of momentum flux in the wave trough-to-crest region to the total depth-integrated value for S_{xx} and S_{xz} as a function of cross-shore depth. For progressive nonlinear water waves, between 40 and 80% of the total momentum flux is carried in the region bound by the wave crest and wave trough.

4.3.3 Stress Gradients and Nearshore Forcing

The previous figures showing vertical profiles of radiation stress components provide valuable information about the distribution of momentum flux produced by nonlinear shoaling waves. Although these radiation stress profiles present useful information concerning the nonlinear distribution of momentum, it is the gradients of radiation and shear stresses that drive nearshore circulation. The significance of cross-shore gradients of S_{xx} on surf zone forcing in producing setup and undertow has been noted by Longuet-Higgins and Stewart (1964), Svendsen (1984), and more recently by Christensen *et al.* (2002). Similarly, forcing in the longshore direction is proportional to the cross-shore gradient of the longshore component of radiation stress, $\frac{\partial}{\partial x} S_{xz}$ (Dean and Dalrymple, 1991). Shear stress distributions (i.e. $\rho\langle uv \rangle$)

play significant roles in circulation as well, but are commonly implemented as depth-uniform or depth-linear forces acting over the water column (Deigaard and Fredsøe, 1989) if they are considered at all. Rivero and Arcilla (1995) discussed the importance of shear stress distributions in the context of more complex conditions for waves encountering ambient currents and sloping bottoms. Deigaard and Fredsøe (1989) also noted the importance of the term $\rho\langle uv\rangle$ as a necessary mechanism for momentum transfer in non-uniform or unsteady wave conditions and discussed its relative importance in their simplified momentum equation given by Eq. 4–12.

$$\frac{\tau}{\rho} = -2\left\langle U\frac{\partial U}{\partial x}\right\rangle(h-y) - g\left\langle \zeta\frac{\partial \zeta}{\partial x}\right\rangle - Sg(h-y) + \left\langle UV\right\rangle \tag{4–12}$$

where
$\tau =$ shear stress
$U =$ horizontal wave-induced velocity
$V =$ vertical wave-induced velocity
$h =$ average water depth
$y =$ vertical location
$\zeta =$ vertical location of the free surface
$S =$ mean slope of the water surface setup

We have plotted the vertical distribution of radiation and shear stress gradients in Fig. 4–18 to emphasize the three-dimensional nature of these nearshore forcing mechanisms. Cross-shore gradients of the radiation stress components were computed over two adjacent grid locations and then minimally smoothed using a diffusive-type filter. The gradients of the shear stress term $\rho\langle uv\rangle$ were calculated over adjacent grid locations in the vertical direction and were also smoothed as little as necessary to ensure that the structure and magnitude of the profile would be retained, while simultaneously providing sufficiently smooth profiles.

Gradients of s_{xx} shown in Fig. 4–18 represent the distribution of the forcing that is applied in the cross-shore direction and has the dimensional units of a force per unit area, per unit depth. Longuet-Higgins and Stewart (1964) stated that this forcing on the

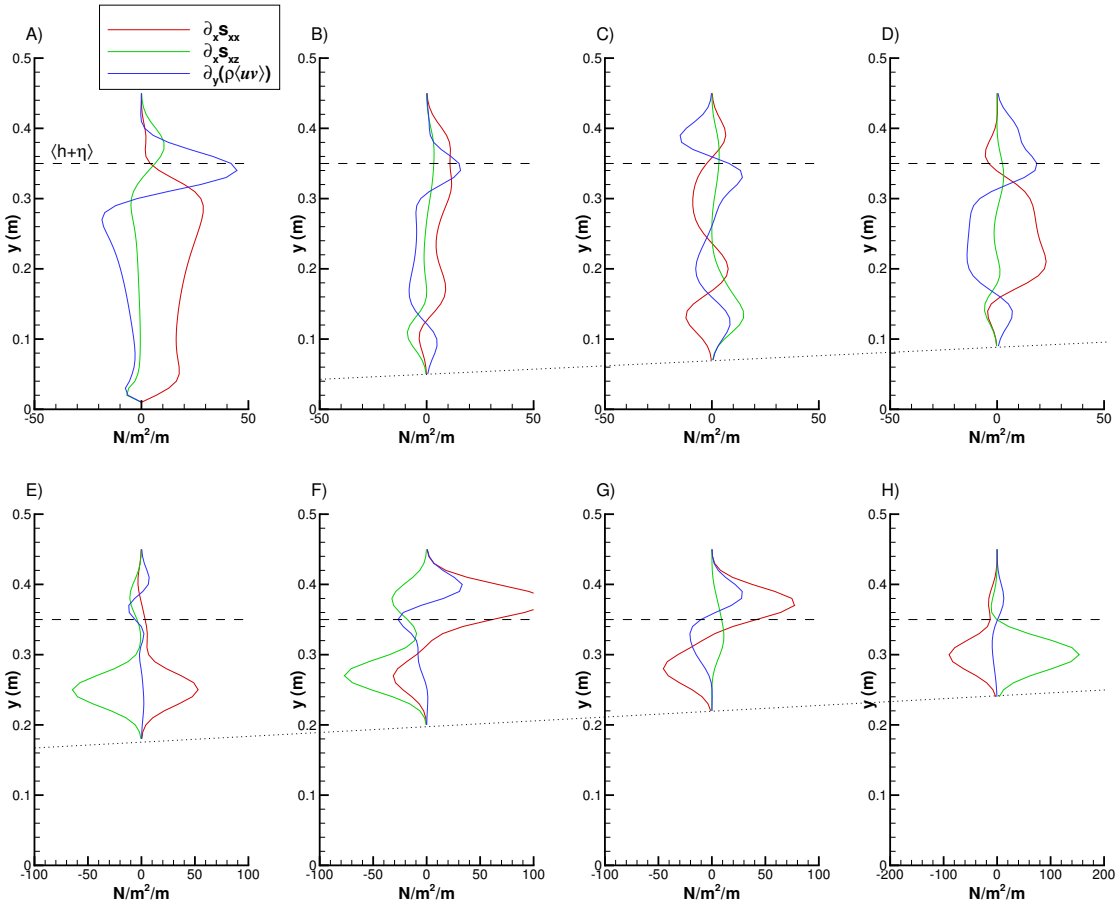

Figure 4–18: The vertical distribution of radiation and shear stress gradients at A) the forcing boundary, B) $h = 0.246$ m, C) $h = 0.226$ m, D) $h = 0.206$ m, E) $h = 0.145$ m, F) $h = 0.124$ m, G) $h = 0.085$ m, and H) $h = 0.069$ m. The dashed line represents the mean water level and the sloping, dotted line represents the approximate location of the bathymetry.

surf zone would be balanced by a gradient in the mean water level (Eq. 4–13).

$$\frac{\partial}{\partial x}\langle\zeta\rangle = -\frac{1}{\rho g h}\frac{\partial}{\partial x}S_{xx} \tag{4–13}$$

This force balance is usually considered in a depth-integrated sense, resulting in the loss of information regarding the vertical distribution of the force balance. Positive values of $\partial_x s_{xx}$ in Fig. 4–18, when depth-integrated , indicate the presence of a shoreward-directed force balancing the wave-induced setdown, while negative values represent a seaward-directed force balancing the setup. Figure 4–18 demonstrates

that there is a unique vertical distribution of the forcing at each cross-shore location, especially in panels F and G where there are significant sign differences above and below the wave trough level. As noted by Dyhr-Nielsen and Sorensen (1970), the balancing forces will not have similar vertical distributions and the inclusion of shear and turbulent stresses and local accelerations for unsteady flows must also be considered to obtain the appropriate force balance over the vertical (Christensen *et al.*, 2002).

The gradients of the longshore radiation stress component ($\partial_x s_{xz}$) plotted in Fig. 4–18 are manifested as longshore-directed forces (per unit area) in the nearshore region (Dean and Dalrymple, 1991). These longshore-directed forces are balanced by bottom shear stresses as well as the resistance to lateral shear over the water column (Longuet-Higgins, 1970). The net magnitude of the resisting forces is found by depth-averaging the profiles of $\partial_x s_{xz}$ in Fig. 4–18 where the sign of the depth-averaged value indicates the direction of action. Depth-averaged values of the $\partial_x s_{xz}$ profiles in Figs. 4–18A–D are small relative to the profiles in panels E–H due to the lower longshore current velocities at the corresponding cross-shore locations. This suggests that the balancing forces would be relatively small at these locations, as well. In panels E and F, however, decreasing magnitudes of s_{xz} result in stronger longshore forcing in the positive z-direction.

Rivero and Arcilla (1995) correctly draw attention to the significance of the term $\langle uv \rangle$ that appears in the depth-averaged momentum equations. Previously, the argument had been made that this value is essentially zero since the horizontal (u) and vertical (v) velocity components are 90° out of phase; this assumption only holds true for steady, periodic, linear waves that are not typically seen in nearshore environments. Recent attempts were made by Rivero and Arcilla (1995) and Deigaard and Fredsøe (1989) to emphasize the importance of including appropriate values and distributions of $\langle uv \rangle$ in momentum equations as this term plays important roles in the

vertical distribution of shear stress as well as wave energy dissipation. The vertical gradient of $\langle uv \rangle$ is shown in Fig. 4–18 at various cross-shore locations where the density constant ρ has been included to compare the relative magnitude of this term to the radiation stress gradients. As they predicted, the gradients of $\rho\langle uv \rangle$ are not negligibly small and in most cases have magnitudes similar to those of the radiation stress gradients seen in Fig. 4–18.

The response to the nearshore forcing produced by gradients in the radiation stress fields is found by integrating the profiles of $\partial_x s_{xx}$ and $\partial_x s_{xz}$ plotted in Fig. 4–18. Relationships for the cross-shore and longshore forcing components are given by Eqs. 4–14 and 4–15, respectively. The term F_x (Eq. 4–14), therefore, is the forcing applied on the surf zone in the cross-shore direction, per unit area. Forcing applied in the longshore direction, per unit area, is given by the component F_z (Eq. 4–15). These two nearshore forcing components are plotted in Fig. 4–19 and provide information concerning the distribution of forcing in the cross-shore domain, the magnitude of each forcing component, and their combined effect. Figure 4–19A demonstrates the magnitude and location of the applied forcing components F_x and F_z, which appear to have bi-modal distributions, with their peaks occurring at similar cross-shore locations. The vectors shown in Fig. 4–19B represent the combined nearshore forcing found by computing the resultant of the two forcing components at each cross-shore location; however, for clarity only one-fifth of the total number of points in the cross-shore domain are represented by this figure.

$$F_x \propto -\frac{\partial S_{xx}}{\partial x} \tag{4–14}$$

$$F_z \propto -\frac{\partial S_{xz}}{\partial x} \tag{4–15}$$

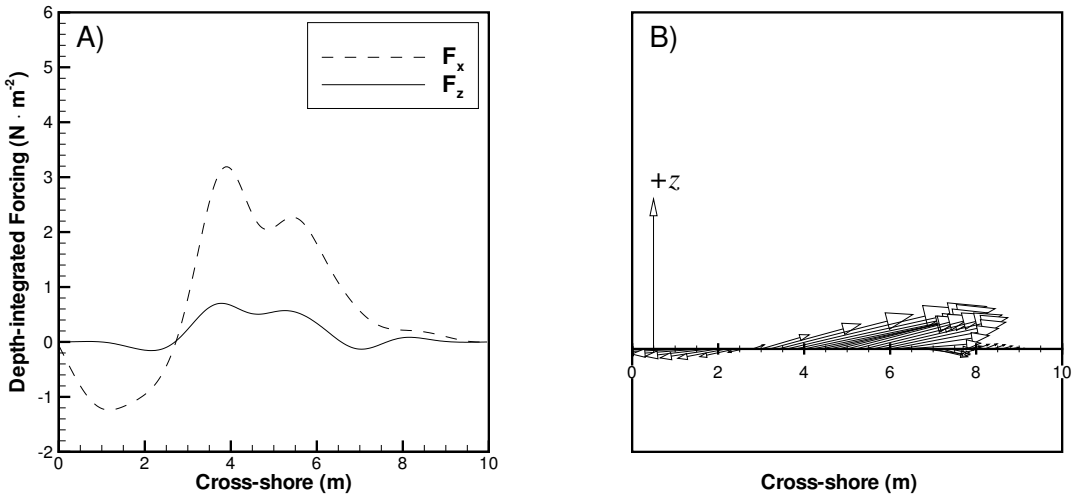

Figure 4–19: Depth-integrated values of the nearshore forcing components F_x and F_z plotted as a function of cross-shore location A) independently and B) as a schematic of the combined nearshore forcing.

CHAPTER 5
SUMMARY

5.1 Applications

SOLA-SURF is a portable CFD model that can be used to study a wide variety of fluid flows. The simplistic nature of the code, evident in both its organization and numerics, enables users with minimal numerical modeling experience to simulate time-dependent flows. Indeed, very little information must be supplied to the model: bathymetry data, wave height, wave period, and the depth at the offshore forcing boundary. In its most basic state this model could be utilized as a teaching or training tool, providing students or other interested individuals a chance to use and manipulate a very simple, yet robustly stable, three-dimensional CFD model. For the more advanced modeler, however, this code serves as a good starting point for building an even more advanced computational tool that can be applied to study more complex problems.

Perhaps the greatest attribute of this Navier-Stokes code is the ability to resolve the time-dependent free surface. This feature could be utilized to study wave diffraction patterns in harbors and basins or around breakwaters and jetties. Providing the model with a three-dimensional bathymetry field, one could study the resulting wave refraction around, for instance, a cuspate beach for both shore-normal and obliquely incident wave fields. Cross-shore and longshore current structures over variable bathymetry could also be investigated for a variety of wave climates.

5.2 Sensitivity

The three-dimensional Navier-Stokes model, SOLA-SURF, provides reasonable estimates of nearshore processes, but relies on both the implementation of the free surface velocity boundary conditions as well as the cell aspect ratio. Care must also be taken when selecting appropriate values of the theta-differencing coefficients in order

to prevent amplitude errors in the wave field and excessive diffusion in the velocity fields. These conditions limit the parameter-space to a range of specific values, but the conditions used in Visser's laboratory experiment were conducive to performing simulations with this model. Waves with lower Iribarren numbers, those in the spilling breaker range, could be more appropriately modeled with SOLA-SURF and the resulting wave transformation would yield better results.

The sensitivity to the free surface velocity boundary conditions is unfortunate, but perhaps a combination between the two methods discussed in Chapter 2 exists, such that improved results could be obtained for both the wave height and velocity fields. Extending these boundary conditions using higher-order differencing schemes is perhaps another viable solution, but ultimately the slope of the free surface will be limited by the cell aspect ratio—a first-order limitation at best. When electing to use SOLA-SURF, it is perhaps best to understand the physical limitations of the model and take them into account when analyzing the results. In this case, we believe that the ability of the model to reproduce the experimental observations precisely is of minor significance in the context of our discoveries. The ability to reproduce approximately accurate or realistic results was a more immediate concern and the comparison of model predictions to laboratory observations, as well as various analytical theories, bolstered our confidence in the applicability of SOLA-SURF to this investigation.

5.3 Discoveries

Performing simulations of Visser's laboratory experiment on uniform longshore currents [Visser (1984); Visser (1991)] with SOLA-SURF has provided new information regarding the vertical distribution of momentum and, more specifically, the horizontal components of radiation stress in the presence of nonlinear shoaling water-waves. While the vertical structure of radiation stress components has been discussed in the literature, particularly in the presence of more realistic waves propagating over variable bathymetry, very little information exists that quantifies

its importance. Our model simulations have lead to the conclusion that in the presence of nonlinear shoaling waves, the majority of momentum flux directed both shoreward (S_{xx}) and alongshore (S_{xz}) is contained within the region bound by the wave trough and crest. Linear theory suggests that roughly one-third of the total momentum flux advected shoreward is found in this region, but our analysis suggests an average value that is roughly twice this amount in the surfzone. Early estimates of radiation stress magnitudes neglected contributions from the wave-induced velocity above the mean water level and, although incorrect in the context of real progressive waves, this methodology continues to be followed.

An interesting, and pertinent, result from this investigation is that the depth-integrated magnitudes of the radiation stress profiles predicted by SOLA-SURF are similar to the magnitudes calculated using analytical solutions provided by Mellor (2003), Longuet-Higgins and Stewart (1964), Dean and Dalrymple (1991), and Dean (1995). This result is pertinent because it provides confidence that the model predictions, while not precise, are accurate. Therefore, nonlinear shoaling waves have radiation stress magnitudes that are relatively similar to the values given by linear theory, but the distribution of momentum flux over the vertical is different. In the context of three-dimensional modeling, this result is important since many circulation models, specifically wave-phase-averaged models, are forced with radiation stress gradient profiles. It has been suggested in the literature that the resulting circulation in these models is highly sensitive to the distribution of forcing over the vertical, but until recently scientists and numerical modelers have had little information regarding more plausible distributions. The analytical expressions given by Mellor (2003), however, tend to underestimate the flux of momentum near, and above, the free surface and overestimate the contribution near the bed in shallow water. This latter result was certainly unexpected and the predicted profiles of radiation stress given by the model show that this feature is not evident. Although the undertow provides some

vertical structure to the radiation stress profile below the trough level, its contribution is typically many times smaller than that found above the mean water level.

Although radiation stress profiles do contribute significantly to the overall flow field, gradients in the radiation stress fields represent the true average cross-shore and longshore forcing in a nearshore system. Analysis of the vertical distribution of radiation stress gradients, however, provided less conclusive information. Gradients of s_{xx} seemed to have unique vertical profiles at each cross-shore location considered in our simulation. Surely, the vertical structure of the mean-flow has much to do with this variability, especially near the bed where the undertow is a dominant flow feature. Some inshore locations yielded profiles of $\partial_x s_{xx}$ that had significant sign differences above and below the mean water level; these locations correspond to areas where the obliquely incident waves are nonlinear, asymmetric, and very steep. On the other hand, the vertical profile of the radiation stress gradient, $\partial_x s_{xx}$, at the forcing boundary suggests that the majority of this cross-shore directed forcing is contained in a depth-uniform distribution below the mean water level, with little contribution above it. As discussed in Chapter 4, this location represents the forcing induced by the monochromatic, sinusoidal wave signal and more or less excludes the Eulerian mean flow. In sharp contrast to the profile of $\partial_x s_{xx}$, the profile of $\partial_x s_{xz}$ at the forcing boundary shows that the majority of the forcing is found in the wave trough-to-crest region with almost no contribution evident below the wave trough level. This distribution is essentially reversed in the location of the peak longshore current, where the largest forcing contribution is found below the mean water level.

APPENDIX A
THETA DIFFERENCING

Predictions offered by numerical models can be sensitive to the finite-differencing scheme used to discretise the governing equations. SOLA-SURF employs theta-differencing in the discretisation of convective flux terms found in the momentum equations (Eqs. 2–2–2–4) and to control the amount of donor cell differencing in the kinematic free surface boundary condition (Eq. 2–5). The discretised forms of the convective flux terms (see Eq. A–1) and the KFSBC (Eq. A–2) are weighted with unique theta coefficients, thereby allowing the user to control the differencing schemes independently.

$$\begin{aligned}\frac{\partial u^2}{\partial x} &= \frac{1}{4\delta x}\Bigg[(u_{i,j,k}+u_{i+1,j,k})^2+\alpha|u_{i,j,k}+u_{i+1,j,k}|(u_{i,j,k}-u_{i+1,j,k})-\cdots \\ &\quad -(u_{i-1,j,k}+u_{i,j,k})^2-\alpha|u_{i-1,j,k}+u_{i,j,k}|(u_{i-1,j,k}-u_{i,j,k})\Bigg] \end{aligned} \tag{A–1}$$

$$\begin{aligned}H_{i,k}^{n+1} &= H_{i,k}^{n}+\delta t\Bigg\{\frac{-1}{4\delta x}\Bigg[(u_{i,jt,k}+u_{i-1,jt,k})(H_{i+1,k}-H_{i-1,k})-\cdots \\ &\quad -\gamma|u_{i,jt,k}+u_{i-1,jt,k}|(H_{i+1,k}-2H_{i,k}+H_{i-1,k})\Bigg]-\cdots \\ &\quad -\frac{1}{4\delta z}\Bigg[(w_{i,jt,k}+w_{i,jt,k-1})(H_{i,k+1}-H_{i,k-1})-\cdots \\ &\quad -\gamma|w_{i,jt,k}+w_{i,jt,k-1}|(H_{i,k+1}-2H_{i,k}+H_{i,k})\Bigg]+\cdots \\ &\quad +h_v v_{i,jt,k}+(1-h_v)v_{i,jt-1,k}\Bigg\}\end{aligned} \tag{A–2}$$

After discovering the sensitivity of the free surface velocity boundary conditions (see Chapter 2), we ran a number of simulations using different values for the

theta-scheme coefficients, α and γ, in order to find the best combination of finite-difference schemes to use in our final simulation. Appropriate values of α, as suggested by Hirt *et al.* (1975) for the two-dimensional SOLA model, are found using the following inequality:

$$1 \geq \alpha \geq \max\left\{\left|\frac{u\delta t}{\delta x}\right|, \left|\frac{v\delta t}{\delta y}\right|, \left|\frac{w\delta t}{\delta z}\right|\right\}.$$

In Hirt *et al.* (1975), a reasonable value of α is said to be 1.2 to 1.5 times greater than the right-hand side of this inequality, but we found this range of values to be too low to produce a stable simulation, given our set of parameters. The lowest value of α that produced a stable simulation was 0.5, which is roughly four times greater than the suggested value using the rule stated above. Values of α below 0.5 resulted in highly dispersive velocity fields that cause the simulation to become unstable, while values of α greater than 0.5 diffused, or smoothed, the velocity fields damping the unsteadiness artificially. While Hirt *et al.* (1975) suggest setting the value of γ equal to α, we found that the stability of the simulations was much less sensitive to the value of γ used. After trying various combinations of α and γ, we found the most agreeable values to be 0.5 and 0.0, respectively. Equations A–3 and A–4 represent the discretised forms of Eqs. A–1 and A–2, respectively, where we have substituted $\alpha = 0.5$ and $\gamma = 0.0$ into the appropriate equations. The sensitivity of the predicted cross-shore wave heights (RMS) to the combination of theta-scheme coefficients is shown in Fig. A–1 for seven of the cases tested.

$$\begin{aligned}\frac{\partial u^2}{\partial x} &= \frac{1}{4\delta x}\Bigg[u_{i+1,j,k}^2 + 2(u_{i,j,k}u_{i+1,j,k} - u_{i,j,k}u_{i-1,j,k}) - u_{i-1,j,k}^2 + \cdots \\ &\quad + \frac{1}{2}\Bigg\{|u_{i,j,k}|(2u_{i,j,k} - u_{i+1,j,k} - u_{i-1,j,k}) + |u_{i+1,j,k}|(u_{i,j,k} - u_{i+1,j,k}) + \cdots \\ &\quad + |u_{i-1,j,k}|(u_{i,j,k} - u_{i-1,j,k})\Bigg\}\Bigg] \qquad \text{(A–3)}\end{aligned}$$

$$H_{i,k}^{n+1} = H_{i,k}^{n} + \delta t \left\{ \frac{-1}{4\delta x}\left[(u_{i,jt,k} + u_{i-1,jt,k})(H_{i+1,k} - H_{i-1,k})\right] - \cdots \right.$$
$$- \frac{1}{4\delta z}\left[(w_{i,jt,k} + w_{i,jt,k-1})(H_{i,k+1} - H_{i,k-1})\right] + h_v v_{i,jt,k} + \cdots$$
$$\left. + (1 - h_v) v_{i,jt-1,k} \right\} \qquad \text{(A–4)}$$

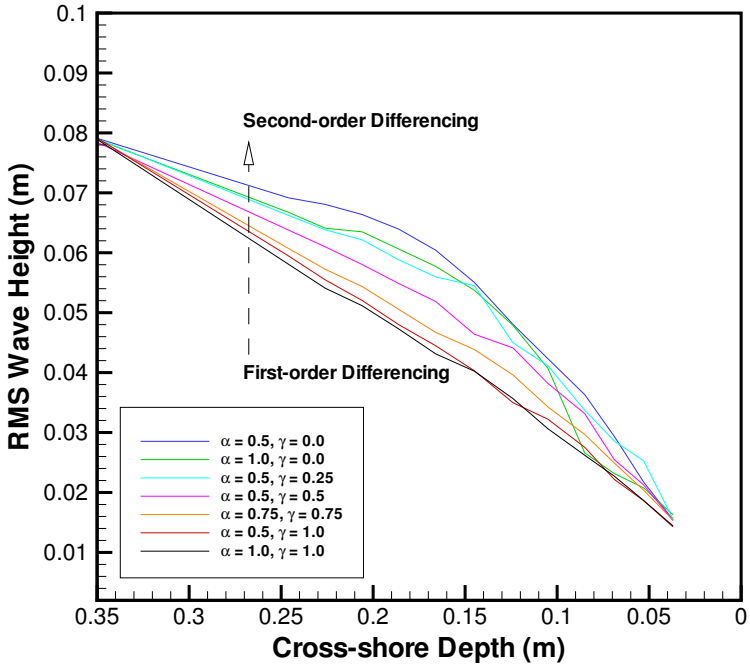

Figure A–1: Effect on numerical diffusion on model predictions. Shown are predicted cross-shore wave heights for different combinations of the theta-scheme discretisation coefficients.

APPENDIX B
CROSS-SHORE MASS BALANCE

In Chapter 4, we briefly touched on the subject of conservation when pointing out features of the velocity profiles taken at various cross-shore locations (Fig. 4–11). Some of the profiles (Figs. 4–11E–4–11H) appeared to be non-conservative: that is, there was an absence of return flow near the bed that would act to balance to shoreward-directed flow near the surface. While it has been noted in the literature that conservation in time-mean velocity profiles should be explicit for purely two-dimensional problems, we expected at least a minor amount of undertow to appear in all of the profiles. The individual velocity profiles plotted in Fig. 4–11, however, only provide information about the mean flow field at one discrete cross-shore location. Figure B–1 shows the time-mean velocity field at a transect taken near the midpoint of the longshore domain. From this figure, we see that there is significantly more structure to the cross-shore circulation than is described by the velocity profiles taken at discrete locations. Just as we discovered in Fig. 4–12 by plotting the time-mean, depth-averaged cross-shore velocity, the mean velocity field between $x = 5$ m and $x = 6.5$ m, shown in Fig. B–1, appears to be directed shoreward with very little return flow near the bed. On the other hand, seaward of $x = 4$ m there is a large, conservative circulation cell that is also evident in the velocity profiles plotted in Figs. 4–11B–4–11D.

It is possible that conservation in this area (5 m $\leq x \leq$ 6.5 m) is satisfied, however, if the excess cross-shore velocity is balanced by some physical storage mechanism. This mechanism can be described through a modified form of the continuity equation (Eq. B–1) that relates the time-dependent free surface to gradients in the velocity fields (Dean and Dalrymple, 2002). Here, we are more concerned with

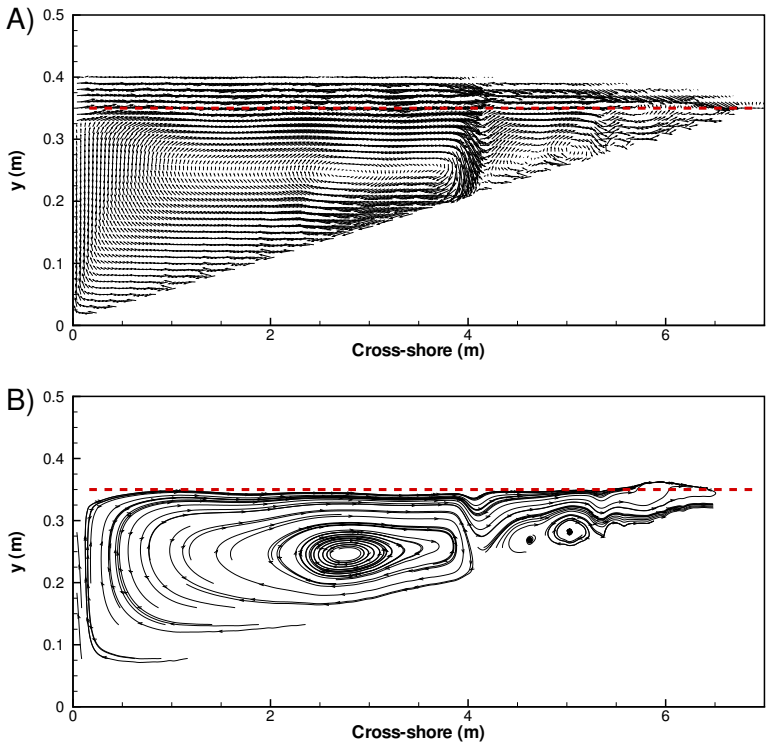

Figure B–1: The time-mean velocity field taken at $z = 2.5$ m and plotted as A) velocity vectors and B) as streamlines. The red, dashed line represents the still water level at initialization.

the cross-shore gradients in the u velocity field since the remaining velocity gradient terms are quite small in comparison.

$$\frac{\partial \eta}{\partial t} + \frac{\partial uh}{\partial x} + \frac{\partial wh}{\partial z} = 0 \tag{B–1}$$

The time-averaged free surface plotted in Fig. B–2B shows that there is a positive displacement of the free surface near the area of the excess cross-shore velocity, which is shown again in Fig. B–2A. In order to see if these two physical processes were spatially related, they were each scaled by their maximum or minimum departure, depending on the sign of the value, thereby non-dimensionalising the two fields.

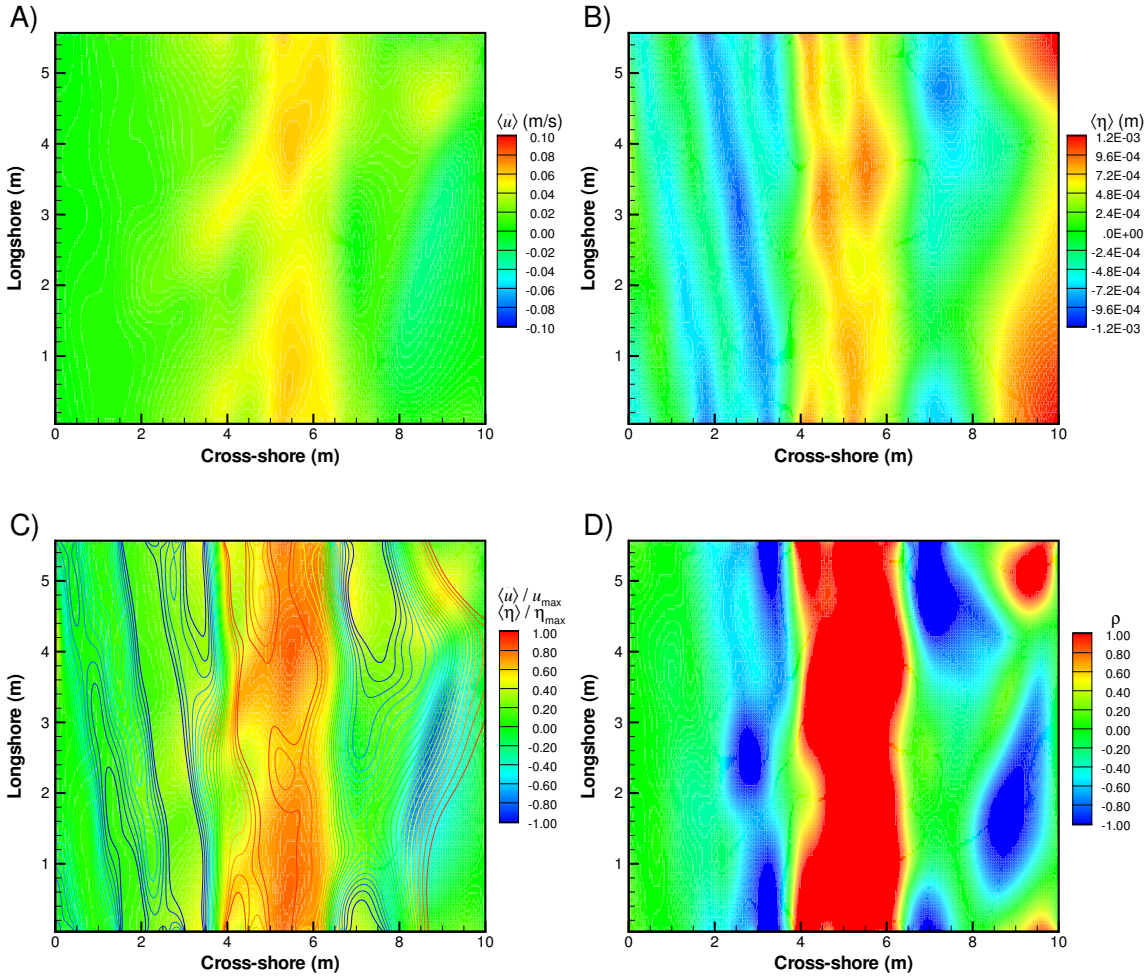

Figure B–2: Spatial features of the average velocity and free surface fields. A contour plot of the time-mean A) depth-averaged cross-shore velocity, B) free surface field, C) scaled velocity (flood) and free surface (lines) fields and D) spatial correlation between the depth-averaged cross-shore velocity and the wave-induced setup and setdown.

Scaling for the velocity and free surface fields was accomplished using the following methodology:

$$
\begin{aligned}
\overline{u}_{max} &= \max[\langle \overline{u}_{x,z} \rangle] \\
\overline{u}_{min} &= \min[\langle \overline{u}_{x,z} \rangle] \\
u^*_{x,z} &= \frac{\langle \overline{u}_{x,z} \rangle}{u_s} \quad \text{where} \quad u_s = \begin{cases} \overline{u}_{max} & \text{for } \langle \overline{u}_{x,z} \rangle > 0 \\ \overline{u}_{min} & \text{for } \langle \overline{u}_{x,z} \rangle < 0 \end{cases}
\end{aligned}
$$

$$\begin{aligned}
\overline{\eta}_{max} &= \max[\langle\overline{\eta}_{x,z}\rangle] \\
\overline{\eta}_{min} &= \min[\langle\overline{\eta}_{x,z}\rangle] \\
\eta^*_{x,z} &= \frac{\langle\overline{\eta}_{x,z}\rangle}{\eta_s} \quad \text{where} \quad \eta_s = \begin{cases} \overline{\eta}_{max} & \text{for } \langle\overline{\eta}_{x,z}\rangle > 0 \\ \overline{\eta}_{min} & \text{for } \langle\overline{\eta}_{x,z}\rangle < 0 \end{cases}
\end{aligned}$$

where $u^*_{x,z}$ and $\eta^*_{x,z}$ are the scaled velocity and free surface fields respectively. This scaling process removes the dimensionality of each variable and results in velocity and free surface fields that vary between -1 and 1:

$$-1 \leq u^*_{x,z} \leq 1 \qquad \text{and} \qquad -1 \leq \eta^*_{x,z} \leq 1\,.$$

The scaled velocity and free surface fields are plotted in Fig. B–2C. We see that maximum positive displacements of the time-averaged free surface field (contour lines) correspond to locations where there is also a maximum, shoreward-directed velocity (contour flood). The correlation between these scaled fields was calculated and the correlation coefficient is plotted in Fig. B–2D. While we know that correlation does not necessarily imply causation, Fig. B–2D suggests that there is a spatial correlation between these two physical processes. Therefore, it is quite possible that the excess depth-averaged cross-shore velocity evident in Fig. B–2A is being *stored* as potential energy in the form of setup, particularly over the shallow sill. A great deal of time was spent attempting to use Eq. B–1 to explain the cause-and-effect relationship of this cross-shore force balance, but the process proved rather difficult; the high degree of spatial and temporal variability made it very difficult to show that this equation is satisfied at each time-step, and over all grid locations, to sufficient precision in the finite difference model.

REFERENCES

ALLEN, J. S., NEWBERGER, P. A. & HOLMAN, R. A. 1996 Nonlinear shear instabilities of alongshore currents on plane beaches. *Journal of Fluid Mechanics* **310**, 181–213.

BADIEI, P. & KAMPHUIS, J. W. 1995 Physical and numerical study of nearshore currents. In *Proc. Coastal Dynamcis*, ASCE, Gdańsk, Poland, 377–388.

BATTJES, J. A. 1974 Computation of set-up, longshore currents, run-up and overtopping due to wind-generated waves. *Comm. on Hydraulics, Rep. 74-2*, Dep. Civil Eng., Delft Univ. of Technology, Delft, The Netherlands.

BOCCOTTI, P. 2000 *Wave Mechanics for Ocean Engineering*. *Oceanography Series* 64. Elsevier, Amsterdam, The Netherlands.

BOWEN, A. J. & HOLMAN, R. A. 1989 Shear instabilities of the mean longshore current, 1. Theory. *Journal of Geophysical Research* **94** (C12), 18023–18030.

BOWEN, A. J., INMAN, D. L. & SIMMONS, V. P. 1968 Wave "set-down" and "set-up." *Journal of Geophysical Research* **73** (8), 2569–2577.

CHAPRA, S. C. & CANALE, R. P. 1998 *Numerical Methods for Engineers*. WCB/McGraw-Hill, Boston, Massachusetts.

CHEN, Q., KIRBY, J. T., DALRYMPLE, R. A., SHI, F. & THORNTON, E. B. 2003 Boussinesq modeling of longshore currents. *Journal of Geophysical Research* **118** (C11), 3362.

CHEN, S., JOHNSON, D. B. & RAAD, P. E. 1995 Velocity boundary conditions for the simulation of free surface fluid flow. *Journal of Computational Physics* **116**, 262–276.

CHORIN, A. J. 1968 Numerical solution of the navier-stokes equations. *Mathematics of Computation* **22**, 745–762.

CHRISTENSEN, E. D., WALSTRA, D. J. & EMERAT, N. 2002 Vertical variation of the flow across the surf zone. *Coastal Engineering* **45**, 169–198.

DEAN, R. G. 1995 Class notes for OCP 6167, Ocean Waves II: Non-linear Theory.

DEAN, R. G. & DALRYMPLE, R. A. 1991 *Water Wave Mechanics for Engineers and Scientists*. World Scientific Press, River Edge, New Jersey.

DEAN, R. G. & DALRYMPLE, R. A. 2002 *Coastal Processes with Engineering Applications*. Cambridge University Press, New York, New York.

DEIGAARD, R. & FREDSØE, J. 1989 Shear stress distribution in dissipative water waves. *Coastal Engineering* **13**, 357–378.

DODD, N., IRANZO, V. & RENIERS, A. 2000 Shear instabilities of wave-driven alongshore currents. *Review of Geophysics* **38** (4), 437–463.

DOLATA, L. F. & ROSENTHAL, W. 1984 Wave setup and wave-induced currents in coastal zones. *Journal of Geophysical Research* **89**, 1973–1982.

DYHR-NIELSEN, M. & SORENSEN, T. 1970 Sand transport phenomena on coasts with bars. In *Proc. of the 12th Int. Conf. on Coastal Eng.* **2**, ASCE, Washington, DC, 855–866.

FLETCHER, C. A. J. 2000 *Computational Techniques for Fluid Dynamics 1*. *Springer Series in Computational Physics*. Springer-Verlag, New York, New York.

GALVIN, C. J. & EAGLESON, P. S. 1965 Experimental study of longshore currents on a plane beach. U. S. Army Coastal Eng. Res. Cent., Vicksburg, Mississippi, Tech. Mem. 10.

HIRT, C. W., NICHOLS, B. D. & ROMERO, N. C. 1975 *SOLA—A Numerical Solution Algorithm for Transient Fluid Flows*, LA-5852 edn. Los Alamos Scientific Laboratory of the University of California, Los Alamos, New Mexico.

IRIBARREN, C. R. & NOGALES, C. 1949 Protection des Ports, Section II, Comm. 4, XVIIth Int. Nav. Congress, Lisbon, 31–80.

LARSON, M. & KRAUS, N. C. 1991 Numerical model of longshore current for bar and trough beaches. *Journal of Waterway, Port, Coastal and Ocean Eng.* **117** (4),ASCE, 326–347.

LONGUET-HIGGINS, M. S. 1970 Longshore currents generated by obliquely incident sea waves, 1. *Journal of Geophysical Research* **75** (33).

LONGUET-HIGGINS, M. S. & STEWART, R. W. 1964 Radiation stresses in water waves; a physical discussion, with applications. *Deep-Sea Research* **11**, 529–562.

MELLOR, G. 2003 The three-dimensional current and surface wave equations. *Journal of Physical Oceanography* **33**, 1978–1989.

MIZUGUCHI, M. & HORIKAWA, K. 1978 Experimental study on longshore current velocity distribution. *Bull. Fac. Sci. Eng. 21*, Chuo Univ., Tokyo, Japan.

OLTMAN-SHAY, J. & HOWD, P. A. 1993 Edge waves on nonplanar bathymetry and alongshore currents: A model and data comparison. *Journal of Geophysical Research* **98**, 2495–2507.

OLTMAN-SHAY, J., HOWD, P. A. & BIRKEMEIER, W. A. 1989 Shear instabilities of the mean longshore current, 2. Field observations. *Journal of Geophysical Research* **94** (C12), 18031–18042.

POPE, S. B. 2000 *Turbulent Flows*. Cambridge University Press, New York, New York.

PUTREVU, U. & SVENDSEN, I. A. 1992 Shear instability of longshore currents: A numerical study. *Journal of Geophysical Research* **97**, 7283–7303.

RENIERS, A. J. H. M., BATTJES, J. A., FALQUÉS, A. & HUNTLEY, D. A. 1997 A laboratory study on the shear instability of longshore currents. *Journal of Geophysical Research* **102** (C4), 8597–8609.

RIVERO, F. J. & ARCILLA, A. S. 1995 On the vertical distribution of $\langle \tilde{u}\tilde{w} \rangle$. *Coastal Engineering* **25**, 137–152.

SOBEY, R. J. & THIEKE, R. J. 1989 Mean flow circulation equations for shoaling and breaking waves. *Journal of Engineering Mechanics* **115** (2), 285–303.

STIVE, M. J. F. & WIND, H. G. 1982 A study of radiation stress and set-up in the nearshore region. *Coastal Engineering* **6**, 1–25.

SVENDSEN, I. A. 1984 Mass flux and undertow in a surf zone. *Coastal Engineering* **8**, 347–365.

SVENDSEN, I. A. & LORENZ, R. S. 1989 Velocities in combined undertow and longshore currents. *Coastal Engineering* **13**, 55–79.

VISSER, P. J. 1984 A mathematical model of uniform longshore currents and the comparison with laboratory data. *Comm. on Hydraulics, Rep. 84-2*, Dep. Civil Eng., Delft Univ. of Technology, Delft, The Netherlands.

VISSER, P. J. 1991 Laboratory measurements of uniform longshore currents. *Coastal Engineering* **15**, 563–593.

XIA, H., XIA, Z. & ZHU, L. 2004 Vertical variation in radiation stress and wave-induced current. *Coastal Engineering* **51**, 309–321.

XIE, L., WU, K., PIETRAFESA, L. & ZHANG, C. 2001 A numerical study of wave-current interaction through surface and bottom stresses: Wind driven circulation in the South Atlantic Bight under uniform winds. *Journal of Geophysical Research* **106** (C8), 16841–16856.

BIOGRAPHICAL SKETCH

I was born and raised in Fort Myers, Florida. As a child most weekends consisted of sailing around San Carlos Bay and Pine Island Sound on my father's boat, often times stopping off at local islands and beaches to play and relax. Occasionally my parents would take my sister and me on longer trips: weekend journeys to Naples or Marco Island and even week-long trips to the Dry Tortugas. I logged my first long distance cruise when I was just a few months old, thus beginning my fascination with oceans, islands, water, and beaches.

Obtaining my SCUBA certification at the age of 13 allowed me to learn about and experience what life is like below the surface of the water. Up until this point, most of my time was spent sailing on the surface of the water with very little knowledge of what was happening below me. Sailing and scuba diving afforded me many opportunities to learn about weather and ocean processes and even from an early age I knew that I wanted to spend my life learning more about both. In the summer of 1996, having just turned 17, I was given the opportunity to do some part-time work for a consulting firm that specialized in coastal and oceanographic engineering. I was exposed to a number of different projects that summer and was immediately fascinated by the work. At the end of the summer, I was quite sure that I had found my passion.

I transfered to Bishop Verot Catholic High School in August 1994 after leaving the public school system at the end of ninth-grade. It was difficult changing schools, but it was certainly one of the best decisions I made as a teenager. Small class sizes and attentive, capable teachers made the learning experience in the classroom that much more enjoyable. While the public school system provided me with a strong educational foundation in science, mathematics, and language arts, the teachers at

Bishop Verot encouraged both critical and creative thinking . . . something I found much more stimulating.

After graduating from Bishop Verot in 1997, I went on to study civil engineering at the University of Florida. I found the faculty to be supportive and many encouraged me to continue my studies after obtaining a bachelor's degree. Since coastal engineering was my true interest, it seemed appropriate to obtain a specialization in this area by continuing on to graduate school. Although I applied to many different programs, after graduating with a Bachelor of Science in Civil Engineering in December, 2001, I received a wonderful offer to continue studying at the University of Florida under Don Slinn. The decision to remain in Gainesville was made even easier by the fact that my girlfriend was working toward obtaining a master's degree in education. Soon after beginning graduate school, I proposed to Shannon and we were married the next year. My wife made graduate school much more tolerable and was always the voice of encouragement at the end of a frustrating day.

Graduate school has been, for the most part, a wonderful experience. In April of 2002 I was awarded a stipend from the Association of Western Universities to perform research at the Naval Research Laboratory at Stennis Space Center for a twelve-week period. During that time, I had the chance to assist in a laboratory experiment at the U.S. Army Corp's Waterway Experiment Station located in Vicksburg, Mississippi, where I learned about particle image velocimetry (PIV) measurement techniques and data collecting. A year later, in October 2003, I assisted scientists from the Naval Research Lab with the NCEX (**N**earshore **C**anyon **Ex**periment) field experiment in La Jolla, California. The opportunity to assist in laboratory and field experiments, combined with traditional learning in the classroom, has enriched my education and has allowed me to apply theoretical science to explain real and observed processes.

MODEL PREDICTIONS OF RADIATION STRESS PROFILES FOR NONLINEAR SHOALING WAVES

Bret M. Webb
(352) 392–9537 ext. 1414
Department of Civil and Coastal Engineering
Chair: Donald N. Slinn
Degree: Master of Science
Graduation Date: December 2004

The state of Florida relies heavily on tourism to support local economies, especially in coastal areas where beaches draw millions of visitors. The coastal regions of Florida are densely populated, with nearly 80% of the state's residents living near a coastal shoreline. Beaches also serve as Florida's first line of defense against damaging storm waves generated by strong winter storms and hurricanes. The stability and topographical evolution of beaches, therefore, is of importance to both the economy of the State and the safety of its residents. The results of this investigation provide new, significant information about the distribution of wave energy in nearshore waters: an important component in the study and numerical modeling of nearshore circulation, which drives sediment transport in the coastal zone. Characteristics of this transport ultimately determine the geometry of a beach and evolution of the nearshore topography over both short and long time scales.